In compliance with the
Canadian Privacy Legislation
some supporting forms
may have been removed from
this dissertation.

While these forms may be included
in the document page count,
their removal does not represent
any loss of content from the dissertation.

University of Alberta

Topography Representation and the Description of JEBAR

by

Mark Cheeseman

A thesis submitted to the Faculty of Graduate Studies in partial fulfilment of the requirements for the degree of Master of Science

Department of Earth and Atmospheric Sciences

Edmonton, Alberta
Fall 2003

National Library of Canada
Acquisitions and Bibliographic Services
395 Wellington Street
Ottawa ON K1A 0N4
Canada

Bibliothèque nationale du Canada
Acquisisitons et services bibliographiques
395, rue Wellington
Ottawa ON K1A 0N4
Canada

Your file Votre référence
ISBN: 0-612-87734-5
Our file Notre référence
ISBN: 0-612-87734-5

The author has granted a non-exclusive licence allowing the National Library of Canada to reproduce, loan, distribute or sell copies of this thesis in microform, paper or electronic formats.

The author retains ownership of the copyright in this thesis. Neither the thesis nor substantial extracts from it may be printed or otherwise reproduced without the author's permission.

L'auteur a accordé une licence non exclusive permettant à la Bibliothèque nationale du Canada de reproduire, prêter, distribuer ou vendre des copies de cette thèse sous la forme de microfiche/film, de reproduction sur papier ou sur format électronique.

L'auteur conserve la propriété du droit d'auteur qui protège cette thèse. Ni la thèse ni des extraits substantiels de celle-ci ne doivent être imprimés ou aturement reproduits sans son autorisation.

Canada

University of Alberta

Library Release Form

Name of Author: *Mark Cheeseman*

Title of Thesis: *Topography Representation and the Description of JEBAR*

Degree: *Master of Science*

Year this Degree Granted: *2003*

Permission is hereby granted to the University of Alberta library to reproduce single copies of this thesis and to lend or sell such copies for private, scholarly or scientific purposes only.

The author reserves all other publication and other rights in assoication with the copyright in the thesis, and except as herein before provided, neither the thesis nor any substantial portion thereof may be printed or otherwise reproduced in any material form whatever without the author's prior written permission.

June 10, 2003

University of Alberta

Faculty of Graduate Studies and Research

The undersigned certify that they have read, and recommend to the Faculty of Graduate Studies and Research for acceptance, a thesis entitled Topography Representation and the Description of JEBAR submitted by Mark Cheeseman in partial fulfillment of the requirements for the degree of Master of Science.

_____

_____

_____

_____

Dr Moritz Heimpel

May 28/03

Abstract

Partial-cell topographic representation differs from the traditional full-cell representation in that the height of the bottommost grid cells can be altered so as to better approximate bottom topography. Ocean models employing this method have displayed an improved resolution of large-scale circulation patterns while experiencing only a small increase in computational costs (Myers, 2002; Käse and Stammer, 2001; Pacanowski and Gnanadesikan, 1998).

The Joint Effect of Baroclinicity and Relief (JEBAR) can be explicitly written as the Jacobian of topography and ocean-bottom pressure or implicitly represented as a collection of terms involving ocean-bottom velocities and topography gradients. With both JEBAR descriptions relying heavily on topography, it is expected that an improved topographic representation will lead to a more accurate numerical description of JEBAR. This premise is tested by determining the overall balance of two vorticity equations (one containing an explicit JEBAR term and one assuming an implicit representation) for the subpolar North Atlantic region. No significant basin-wide differences are seen between the two JEBAR descriptions utilizing full and partial-cell implementations of the same regional ocean model. Small-scale and regional-scale differences are seen between the topographic representations.

Table of Contents

Abstract ii

List of Figures v

1 Introduction 1
- 1.1 Improving topography representation . . . 7
  - 1.1.1 Hybrid models . . . 8
  - 1.1.2 Modified-cell approach . . . 10
- 1.2 Partial-cell topography representation . . . 15
- 1.3 Finite-volume discretization scheme . . . 18
  - 1.3.1 Conserved equations . . . 19
  - 1.3.2 Equation of continuity . . . 20
  - 1.3.3 Equation of conservation for linear momentum . . . 27
  - 1.3.4 Employing partial cells . . . 35
  - 1.3.5 Discretized hydrostatic primitive equations . . . 37
  - 1.3.6 Order of accuracy in vertical discretizations . . . 39
- 1.4 Numerical errors introduced by partial-cells . . . 39

2 The JEBAR Term 42
- 2.1 JEBAR's origins . . . 42
- 2.2 JEBAR applications . . . 46
- 2.3 Describing JEBAR . . . 47
  - 2.3.1 JEBAR as a vorticity correction . . . 48
  - 2.3.2 Decomposing JEBAR . . . 50
  - 2.3.3 Summary . . . 53

3 Design of experiments 55
- 3.1 SPOM settings . . . 56
  - 3.1.1 Background . . . 56
  - 3.1.2 Modelled domain . . . 59

3.1.3 Boundary conditions 60
3.1.4 A comment about depth-averaging 63

4 Results **65**
4.1 Balances of the Vorticity Equations 66
4.1.1 Barotropic Vorticity Equation 67
4.1.2 Vorticity Equation for the Depth-Averaged Flow 76
4.2 Overall Balance of Vorticity Equations at Specific Geographical Sites 79
4.2.1 Eirik Ridge 79
4.2.2 Hamilton Bank 87

5 Summary **101**

Appendix - JEBAR Derivations in Spherical Coordinates **110**
A.1 Necessary Definitions 110
A.2 Vorticity of the depth-averaged flow 112
A.3 Forming the barotropic vorticity equation 114
A.4 Vorticity correction relation 115

List of Figures

1.1 Representation of a topographic slope using a full-cells. 3
1.2 Same full-cell representation as in Figure 1.1 with the horizontal resolution doubled. 4
1.3 Adcroft's barotropic flow experiment with A) original resolution, B) doubled horizontal resolution and C) doubled vertical resolution. . . 5
1.4 Vertical discretization in Gerdes' BBLM. 9
1.5 Topography representation of a gaussian bump using (a) full cells and (b) partial cells. 13
1.6 Two possible shapes of a bottommost grid cell in a piecewise-linear model. 17
1.7 An arbitrary volume Ω that is subdivided into smaller volumes Ω_1-Ω_3. 19
1.8 Cartesian mesh designs used for our discretization exercise. 23
1.9 Example of a rectangular finite volume cell found in the mesh designs of Figure 1.8. 24
1.10 Two adjacent finite-volume cells with different cell heights. 36

4.1 Full-cell representation of the subpolar gyre domain used in our experiments. 65
4.2 Computed sum of the individual terms in the barotropic vorticity equation for the entire subpolar gyre domain. 68
4.3 Computed magnitudes for the Coriolis term arising in the barotropic vorticity equation. 72
4.4 Computed magnitudes for the depth-averaged meridional current velocities in the sub-polar gyre domain. 73
4.5 Computed magnitudes for the non-linear advection term arising in the barotropic vorticity equation. 74
4.6 Computed magnitudes for the external stress terms (wind and bottom friction) found in the barotropic vorticity equation. 75
4.7 Computed sum of the individual terms arising in the vorticity equation for the depth-averaged flow. 77

4.8 Computed magnitudes for the explicit JEBAR term appearing in the vorticity equation for the depth-averaged flow. 78
4.9 Barotropic flow around Eirik Ridge predicted by current data from the Sub-Polar Ocean Model. 83
4.10 Sum of the individual terms arising in the barotropic vorticity equation around Eirik Ridge. 84
4.11 Magnitudes of the three dominant terms in the barotropic vorticity equation along a zonal cross-section (59.1667°N). The cross-section is denoted by the red dotted line in Figure 4.10. 85
4.12 Computed sum of the individual terms arising in the vorticity equation for the depth-averaged flow around Eirik Ridge. 89
4.13 Magnitudes of the four dominant terms in the vorticity equation for the depth-averaged flow along a zonal cross-section (59.1667°N). The cross-section is denoted by the red dotted line in Figure 4.12. 90
4.14 Computed ocean-bottom pressure gradient using predicted tracer and topography data from the Sub-Polar Ocean Model around Eirik Ridge. 91
4.15 Barotropic flow about the Hamilton Bank region predicted by current data from the Sub-Polar Ocean Model. 92
4.16 Computed sum of the individual terms arising in the barotropic vorticity equation around Hamilton Bank. 94
4.17 Magnitudes of the three dominant terms in the barotropic vorticity equation along a zonal cross-section (55.833°N). The cross-section is denoted by the red dotted line in Figure 4.16. 95
4.18 Computed sum of the individual terms arising in the vorticity equation for the depth-averaged flow around Hamilton Bank. 98
4.19 Magnitudes of the four dominant terms in the vorticity equation for the depth-averaged flow along a zonal cross-section (55.833°N). The cross-section is denoted by the red dotted line in Figure 4.18. 99
4.20 Gradient of ocean-bottom pressure around Hamilton Bank. 100

Chapter 1

Introduction

A number of popular ocean general circulation models (OGCMs) use the z-level design with a well-known example being the Modular Ocean Model (MOM)(Pacanowski and Griffies, 2000). The popularity of this design stems from a number of factors:

Simplicity The utilisation of a uniform grid cell geometry and a simplified physical model allows for relatively easy implementation and modification of the design.

Development Thirty years of usage have led to a great deal of development and innovation in the OGCM design. These innovations include the application of improved memory usage, incorporation of parallel computing, and accomodation for different topography representations. Various variants of the traditional z-level design have been created such as MOMA (Udall, 1996) and the MIT z-coordinate model (Marshall et al., 1997).

Realism The governing hydrostatic primitive equations (Haidvogel and Beckmann, 1999) can create realistic depictions of actual patterns provided an appropriate

resolution is used. For instance, the hydrostatic approximation in most cases is a fairly accurate representation of real ocean pressure variations (Haidvogel and Beckmann, 1999). Parameterization has been applied to represent diffusion and friction processes. Appropriate closure techniques have also been included.

The practicality of a z-level OGCM depends on its vertical discretization scheme. Figure 1.1 illustrates a typical vertical discretization of a modelled basin into depth layers. Notice that each individual layer maintains its own uniform thickness. In the bottom-most depth layers, this results in an altered representation of the ocean-bottom topography. More specifically, bottommost grid cells that are partially filled with land are changed to either completely fluid filled cells or completely land filled cells. This process alters modelled ocean-bottom depths, topographic slopes, and volumes of individual water columns.

Fitting an ocean-bottom surface to the depth layers of constant thicknesses in a z-level OGCM leads to what is known as "staircase topography"(Adcroft et al., 1997). Staircase topography refers to the process by which steep slopes in real bottom topography are represented by a series of large steps. An example of this effect is seen in Figure 1.1 where a simple topographic slope is depicted using a standard full-cell staggered vertical discretization (i.e. Different depth layers have different thicknesses but each layer's thickness remains uniform).

The staircase topography effect is very sensitive to changes in horizontal resolution. This effect is illustrated in Figure 1.2 where we have the same vertical discretization

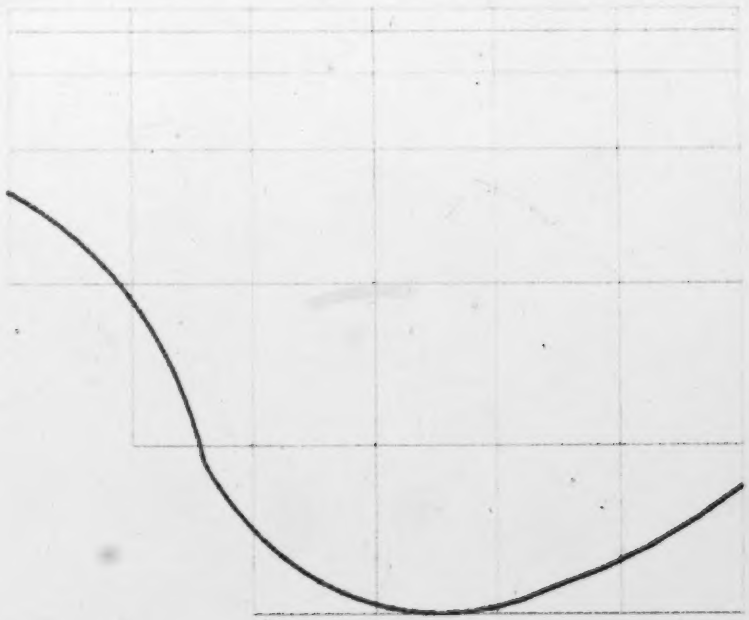

Figure 1.1: Representation of a topographic slope using a full-cells.

used in Figure 1.1 but the horizontal resolution has been doubled. Grid cells are considered to be land-filled when fifty percent or more of the cell is occupied by the true topography. The topographic slope is depicted in a step-like fashion in both cases. Notice that in the first case (Figure 1.1) there is a systematic overestimation of the individual water columns above the slope. With the higher horizontal resolution, there is now an underestimation of the individual water columns above the large topographic slope.

Staircase topography can also introduce unwanted physical and numerical effects. Adcroft et al. (1997) perfomed a numerical experiment where MOM was used to

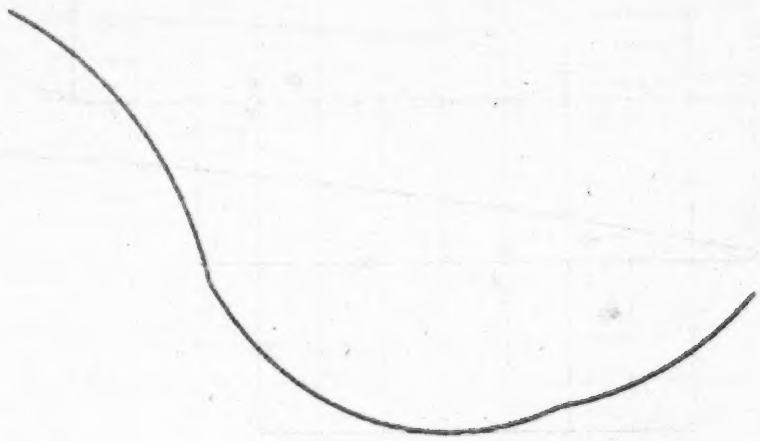

Figure 1.2: Same full-cell representation as in Figure 1.1 with the horizontal resolution doubled.

depict barotropic flow over an ocean-bottom with a gentle upwards slope. The staircase topography representation of the slope was simply a large step as seen in Figure 1.3A. It was found that laterally flowing water would impact the step barrier and produce gravity waves that perturbed most of the lateral flow. Increasing the horizontal resolution alone simply moved the location of the step barrier while increasing the vertical resolution alone just increased the number of step barriers present thereby intensifying the gravity wave problem.

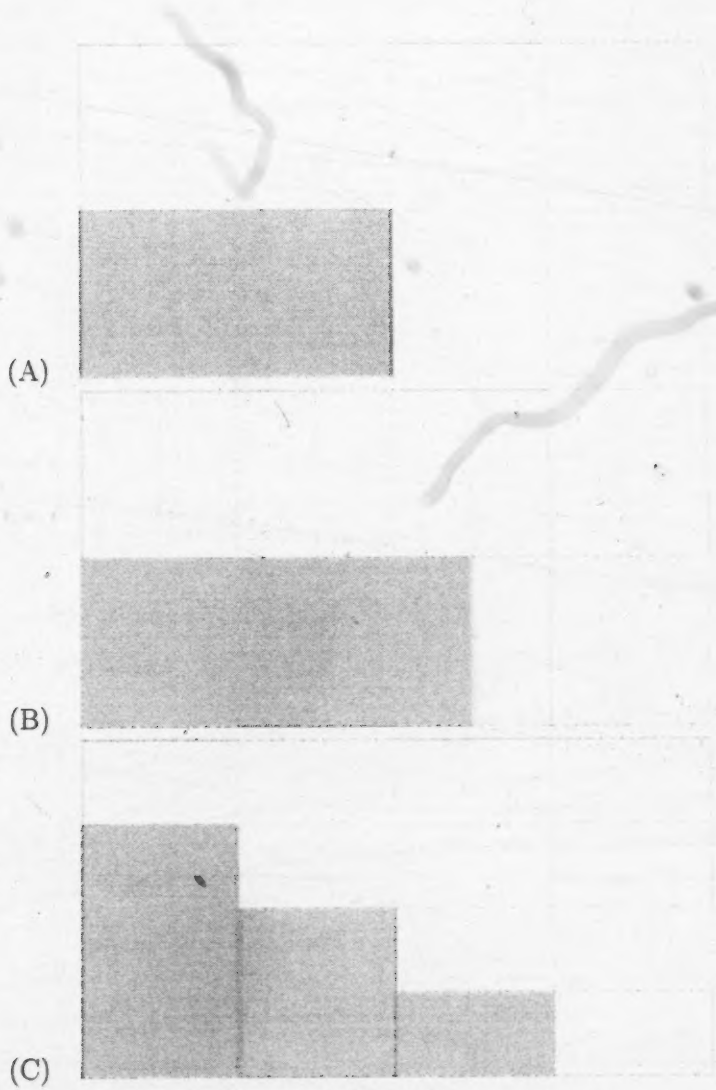

Figure 1.3: Adcroft's barotropic flow experiment with A) original resolution, B) doubled horizontal resolution and C) doubled vertical resolution.

Increasing both the horizontal and vertical resolution may be the intuitive response to the staircase topography problem. Unfortunately this response has two major drawbacks. One, even a small increase in resolution can lead to a significant increase in computational costs. Two, a numerical stability constraint may restrict the spatial resolution one wishes to use. For example, take the simple one-dimensional advection equation

$$\frac{\partial u}{\partial t} + c\frac{\partial u}{\partial x} = 0 \tag{1.1}$$

where $u = u(x,t)$ and c is a scalar. Utilizing a forward-in-time and centered-in-space finite-difference scheme(Haidvogel and Beckmann, 1999) on Equation 1.1 produces the discrete equation

$$u_j^{n+1} - u_j^n = -c\frac{\Delta t}{2\Delta x}\left(u_{j+1}^n - u_{j-1}^n\right) \tag{1.2}$$

with u_j^n being the value of u at gridpoint j during timestep n. Subsituting in a wave-like solution form into Equation 1.2 (i.e. $u_j^n = A^n e^{ij\phi}, \quad i \equiv \sqrt{-1}$) yields

$$\left(A^{n+1} - A^n\right) e^{ij\phi} = -c\frac{\Delta t}{2\Delta x}\left(e^{i\phi} - e^{-i\phi}\right) A^n e^{ij\phi}$$

Dividing through by $A^n e^{ij\phi}$ gives

$$\begin{aligned}\left(\frac{A^{n+1}}{A^n} - 1\right) &= -c\frac{\Delta t}{2\Delta x}\left(e^{i\phi} - e^{-i\phi}\right) \\ &= -c\frac{\Delta t}{\Delta x}\left(i\sin\phi\right)\end{aligned} \tag{1.3}$$

For the applied finite-difference scheme to be stable we require that no artificial amplification occurs in the approximate solution between successive timesteps. I.e.

$$\|\frac{A^{n+1}}{A^n}\| \equiv \|G\| \leq 1$$

Therefore Equation 1.3 can be rewritten as

$$G = 1 - i\sigma \sin\phi$$

Using the stability requirement $\|G\| \leq 1$ we have

$$\sqrt{1 - (\sigma \sin\phi)^2} \leq 1$$

$$1 - (\sigma \sin\phi)^2 \leq 1$$

$$\|\sigma \sin\phi\| \leq 1$$

$$\sigma \leq 1 \tag{1.4}$$

The stability criterion that $\sigma \leq 1$ is called the Courant-Friedrichs-Lewy criterion (Hirsch, 1990). Therefore one must be careful to ensure that any spatial resolution change upholds

$$\|c\frac{\Delta t}{\Delta x}\| \leq 1$$

assuming that the timestep remains unaltered.

1.1 Improving topography representation

Two principal approaches have been developed to improve topography representation in z-level OGCMs: the use of hybrid models and the application of modified-cell

grid meshes. Both approaches have the common goal of reducing the staircase topography effect.

1.1.1 Hybrid models

In a hybrid model the z-level design is merged with another OGCM design. A common approach is to use a hybrid ocean model design using a combination of height and sigma-coordinate(Phillips, 1957) discretization. Here the interior depth layers of the modelled basin are vertically discretized using the traditional height coordinate while a sigma surface(s) is used to describe the bottommost depth layer. Hybrid ocean models that utilize such a vertical discretization have become known as bottom boundary layer models(BBLMs).

One example is the BBLM by Gerdes (1993) shown in Figure 1.4 where interior depth layers are vertically discretized using the height coordinate while the deeper depth layers are vertically discretized using sigma surfaces. k is the depth layer index and the squares represent the center grid point in each mesh cell. In Gerdes' model the current velocities (u,v) are determined along the center of the cell face common to two adjacent cells. The final sigma surface lies on the ocean floor. Beckmann and Döscher (1997) modified Gerdes' design so that only one sigma layer of constant thickness is used. More recently, Killworth and Edwards (1999) have released a BBLM where the thickness of the single sigma layer can spatially and temporally vary.

The z-level/sigma-coordinate hybrid design offers a few advantages. Firstly, the

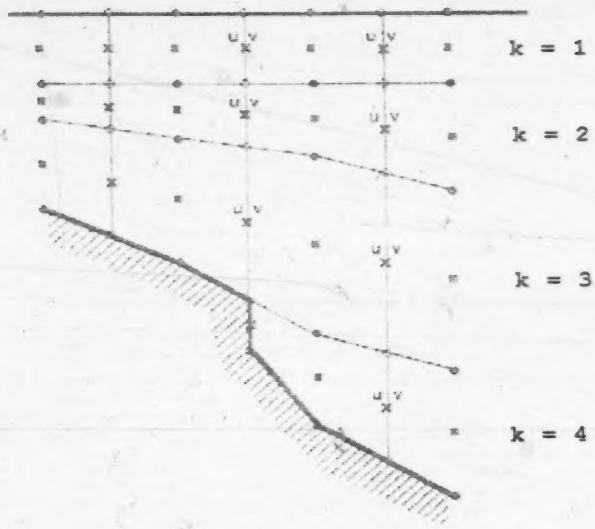

Figure 1.4: Vertical discretization in Gerdes' BBLM.

terrain-following sigma surfaces can accurately represent ocean-bottom topography, especially small-inclined topographical features that are lost in the traditional z-level model design. Secondly, since the last sigma surface lies on the ocean-bottom surface, one can impose exact bottom boundary conditions. And finally, with an explicit bottom boundary layer present, one can introduce parameters that represent specific physical processes inside the boundary layer such as tracer diffusion.

In the traditional z-level design all depth layers are horizontal. The finite-difference cells that comprise each depth layer each contain a centrally located data point. For each depth layer, these data points form a horizontal plane that is called a *depth surface*. In the hybrid design the depth surfaces lose their horizontal form at the interface where z-coordinate vertical discretization ends and the sigma-coordinate vertical dis-

cretization begins. This loss of horizontal uniformity can invalidate the hydrostatic approximation used in the model's governing equations producing incorrect lateral flows. (I.e. Vertical flow becomes more significant in the circulation description with non-horizontal depth surfaces (Haney, 1991; Mellor and Oey, 1993). As a result, the hydrostatic approximation of the Navier-Stokes equation for vertical momentum fails as the neglected momentum terms become more significant.) Steep topographic gradients amplify this numerical problem by creating further horizontal nonuniformity in the depth surface. In a sigma-coordinate model, these pressure gradient errors are propagated throughout the entire water column. Smoothing of the bottom sigma layer can alleviate the problem but obviously results in poorer topographic representation.

Another problem is that the depth surfaces formed inside the sigma depth layers tend to intersect more isopycnals which in turn brings about spurious diapycnal mixing. This unrealistic mixing can be intensified by the before-mentioned incorrect horizontal pressure gradients. While the magnitude of both numerical errors can be reduced by appropriate correction terms, their effects generally can not be totally eliminated.

1.1.2 Modified-cell approach

A second approach to improve ocean-bottom topography representation is to modify the shape of the bottom-most grid cells so that they fit the ocean-bottom surfaces better. Two methods have been explored that implement this approach: the partial-

cell (Adcroft et al., 1997; Pacanowski and Gnanadesikan, 1998) and piecewise-linear-cell (Adcroft et al., 1997) methods. In the partial-cell method the bottom-most grid cells retain their rectangular shape but change their height so that they better approximate the ocean-bottom boundary. This lessens the "step-like" feature of modelled topography and reduces artificially induced gravity wave noise. In the piecewise-linear-cell method the bottom-most grid cells are "shaved" so that they better fit the topographical surface. Here the grid-cell bottoms need not be horizontal. Thus, the modelled topography is more smooth and continuous compared to the full-cell and partial-cell representations. As a result, artificial gravity wave noise is mostly eliminated except in areas with severe topographic variations. Figure 1.5 illustrates the difference between the partial-cell and the original full-cell methods in representing a sea-mount.

Partial-cell ocean models tend to produce much better topography representation for a given increase in horizontal resolution due to their large vertical scaling ability. Interior depth layers are not modified- only the bottom-most cells and depth surfaces are altered. Therefore either method can be easily implemented. Their property of fitting to the ocean-bottom surface also creates a better approximation of the volume in individual water columns. Unfortunately, piecewise-linear topographic representation does incur greater computational expenses arising from the arbitrary orientation of the bottom cell face of the bottommost grid cells. Partial-cell representation is less complex and thereby less computationally expensive. Adcroft et al. (1997) con-

ducted a series of numerical experiments (flow around a seamount, barotropic flow along a slope, overflow in a sloping channel) to compare the effects of partial-cell and piecewise-linear-cell topographic representation. They found that both representations produced similar improvements over the traditional full-cell representation approach. Also, they showed that as horizontal resolution increased the two computed solutions become increasingly identical.

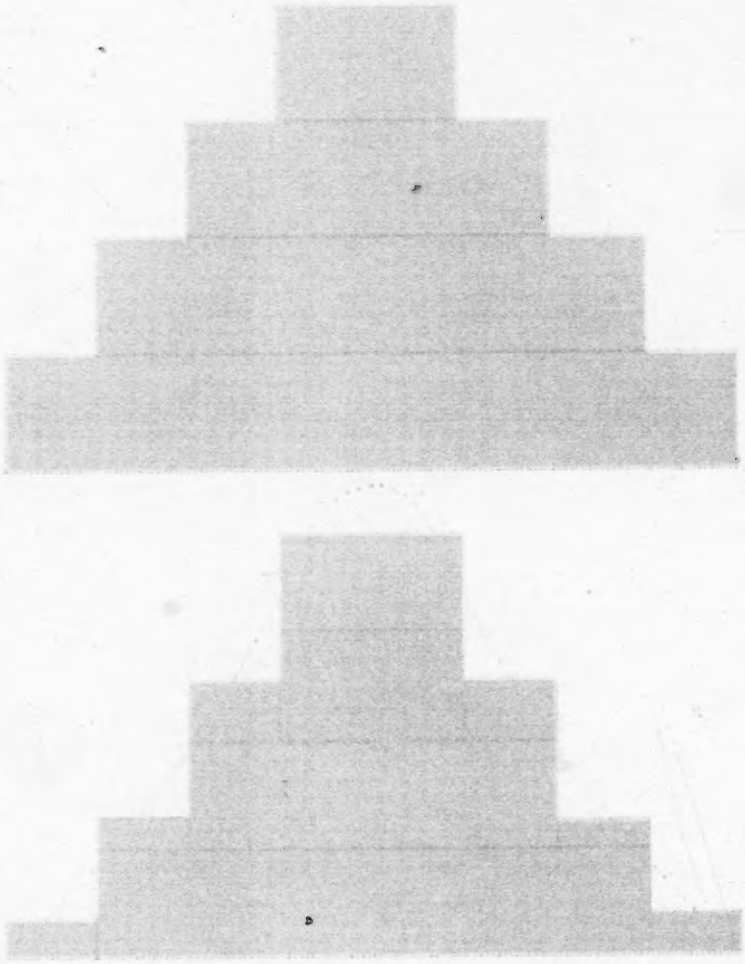

Figure 1.5: Topography representation of a gaussian bump using (a) full cells and (b) partial cells.

In depth layers that contain modified grid cells, the depth surfaces become non-horizontal as in the case of BBLMs. As a result the modified-cell approach suffers from the same horizontal pressure gradient and spurious diapycnal mixing numerical errors. The non-horizontal shape of the depth surfaces can also bring about numerical errors in the equation of state of the modelled basin. For example, the use of modified cells in the MOM ocean model can introduce errors in the coefficients of its polynomial approximation of the UNESCO equation of state. This results in the formation of density anomalities that bring about velocity errors.

The previously mentioned horizontal pressure gradient errors can also arise in sigma-coordinate ocean models. In the sigma-coordinate model design these pressure gradient errors would propagate upwards and influence other depth layers (Haney, 1991; Mellor and Oey, 1993). However in the modified-cell approach these errors are limited to the bottom depth layers containing modified grid cells. Additionally, correction terms can be applied to reduce the undesirable effects of the pressure gradient and equation of state errors (Pacanowski and Gnanadesikan, 1998). A more detailed explanation of the correction term for the horizontal pressure gradient error will be given in a later section.

A partial-cell model using a finite-volume discretization scheme (Hirsch, 1990) will have the same discrete governing equations in the interior depth layers as in a full-cell model employing a finite-difference discretization scheme and are second-order accurate. In the bottommost depth layers, these equations are only first-order accurate in

a partial-cell model. However, since partial cells improve topography representation (which is a zeroth-order problem), the drop in accuracy in the governing equations is considered to be acceptable and the model is assumed to remain second-order accurate overall.

1.2 Partial-cell topography representation

The popularity of the partial-cell method has grown over recent years. Its effectiveness has been the focus of several numerical experiments (Adcroft et al., 1997; Pacanowski and Gnanadesikan, 1998). It has been implemented in full-scale models of the Indian Ocean(Pacanowski and Gnanadesikan, 1998) and the sub-polar region of the North Atlantic (Myers, 2002; Käse and Stammer, 2001). Partial-cell topography representation is also now offered in the latest version of MOM by Pacanowski et al (2000).

The biggest advantage of the partial-cell method is its efficiency in improving topography representation without dramatically increasing computational costs. Pacanowski and Gnanadesikan (1998) estimated that their partial-cell model of the Indian Ocean incurred only a ten percent increase in integration time over their corresponding full-cell model. The newest version of MOM (Pacanowski and Griffies, 2000) can utilize partial-cell topography representation with only a reportedly ten to fifteen percent increase in integration time over the original full-cell representation. The partial-cell model of the sub-polar North Atlantic by Myers (2002) displayed improved represen-

tation of current structures and mode water dispersal over his corresponding full-cell model with an increase of only six percent in computational costs. This increase is approximately the same as that encountered when the total number of depth layers in the modelled basin is increased from thirty-six to fourth-one.

A second advantage is the relatively simple finite-volume discretization scheme applied on the governing equations of the z-level OGCM used in both modified-cell approaches (Adcroft et al., 1997). For interior depth layers, where the depth surfaces are horizontal, the finite-volume discretization of the governing equations is exactly the same as finite-difference discretizations (This will be explicitly shown in the next section). Thus implementing a modified-cell approach in an existing z-level OGCM is relatively easy.

Determination of the volume flux through a grid cell and of surface flux through each individual cell face are key components for the before-mentioned finite-volume discretization of the governing equations. These determinations are simple when rectangular grid cells are used (as in the case of full- and partial-cell models). However, in piecewise-linear models, the bottommost grid cells can have a more general parallelepiped shape as illustrated in Figure 1.6.

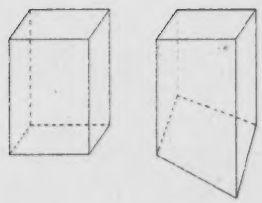

Figure 1.6: Two possible shapes of a bottommost grid cell in a piecewise-linear model.

Volume and surface flux determinations become more complex as grid cell geometry becomes more arbitrary. This leads to a more sophisticated model with higher computational costs. Therefore, although piecewise-linear models better represent topography, partial-cell models have become much more widely accepted with a more tolerable increase in model complexity and computational costs.

1.3 Finite-volume discretization scheme

As stated previously, in the partial-cell method the governing equations are discretized using a finite-volume discretization scheme. Usually these governing equations are the hydrostatic primitive equations (Haidvogel and Beckmann, 1999) which include a simplified version of the Navier-Stokes equations, the hydrostatic approximation, the equation of continuity, an equation of state describing in-situ ocean density, and equations for tracer advection.

In this section we will introduce a finite-volume discretization scheme by applying it to the equation of continuity and a simplified version of the Navier-Stokes equations. The equations will be discretized onto a Cartesian grid where the vertical discretization is stretched. In other words, while each depth layer is horizontally uniform, not all depth layers will have the same thickness. We will also show the differences in the discretizations when full and partial cells are used. A full description of the theory and application of the finite-volume discretization scheme can be found in various sources such as Hirsch (1990) for example. While our explanation of the discretiza-

tion process is fairly complete, it is only a simplification of the actual discretization process used in real OGCMs.

1.3.1 Conserved equations

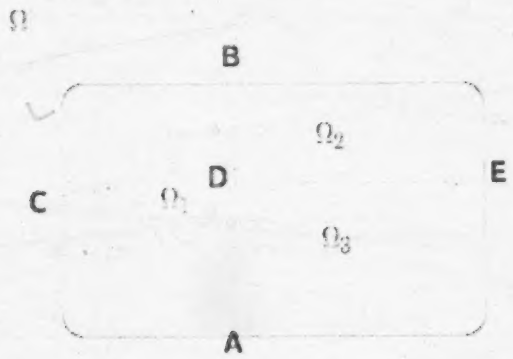

Figure 1.7: An arbitrary volume Ω that is subdivided into smaller volumes Ω_1-Ω_3.

Suppose we have an arbitrary volume Ω as illustrated in Figure 1.7 whose external surface is given by S. The integral conservation law for a scalar quantity inside Ω is

$$\frac{\partial}{\partial t}\int_{\Omega} U\, d\Omega + \oint_{S} \vec{F}\cdot d\vec{S} = \int_{\Omega} Q\, d\Omega \tag{1.5}$$

where U is the amount of the scalar quantity per unit volume, $\vec{F}$ is the amount of quantity flux through the volume's external bounding surface S, $d\vec{S}$ is a normal surface element vector, and Q is any volume sources or sinks of U inside the volume Ω.

One property of Equation 1.5 is that if Ω is subdivided into an arbitrary number

of smaller subvolumes then the sum of the scalar conservation laws for the smaller subvolumes will equal the scalar conservation law of the large volume. Ignoring any sources or sinks inside the subvolumes we have

$$\frac{\partial}{\partial t}\int_{\Omega_1} U\,d\Omega + \frac{\partial}{\partial t}\int_{\Omega_2} U\,d\Omega + \frac{\partial}{\partial t}\int_{\Omega_3} U\,d\Omega$$
$$= -\oint_{ABCA} \vec{F}\cdot d\vec{S} - \oint_{DEBD} \vec{F}\cdot d\vec{S} - \oint_{AEDA} \vec{F}\cdot d\vec{S}$$

For the above equation to be valid, some internal flux values must cancel. For example, subvolume Ω_2 has an internal flux

$$\int_{DE} \vec{F}\cdot d\vec{S}$$

while the subvolume Ω_3 experiences the same flux but in the opposite direction.

$$\int_{ED} \vec{F}\cdot d\vec{S} = -\int_{DE} \vec{F}\cdot d\vec{S}$$

Thus, when we sum up all the fluxes in Equation 1.5 the internal fluxes cancel out. The Navier-Stokes equations and equation of continuity are conserved equations that possess the above property.

1.3.2 Equation of continuity

An important simplification used in OGCMs such as MOM is that the ocean is filled with an incompressible fluid (Haidvogel and Beckmann, 1999). That means that the volume of a parcel of water, $\delta\Omega$, subjected to a velocity field $\vec{v}$ will be conserved

(Acheson, 1990). If **S** is the surface of the water parcel then the net volume of water leaving the water parcel is

$$\oint_S \vec{v} \cdot \vec{dS} = 0 \tag{1.6}$$

where $\vec{dS}$ is the outward normal surface vector for the water parcel. Applying Gauss' divergence theorem yields

$$\int_\Omega (\nabla \cdot \vec{v})\, d\Omega = 0$$

Since the incompressibility assumption covers the entire water body, the above relation must hold for all volumes. Eliminating the volume integral leads to the familar equation of continuity.

$$\nabla \cdot \vec{v} = 0 \tag{1.7}$$

Equation 1.6 is a conserved equation and has the same structure as Equation 1.5 except no time dependence is present. Physically, the equation is saying that the sum of all velocity fluxes through the boundary of the water body is zero. Because the equation is conserved we can subdivide our water volume Ω into a number of finite subvolumes $\Omega_i, \quad i \in \{1, \ldots, N\}$. The corresponding discrete equation is then

$$\sum_{sides} \vec{v}_i \cdot \vec{S}_i = 0 \tag{1.8}$$

which states that the sum of all the velocity fluxes through every subvolume Ω_i is zero.

Finite-volume meshes The finite subvolumes can have any arbitrary shape and size but we will impose the two following constraints(Hirsch, 1990) :

i The sum of the subvolumes should equal the volume of the original domain. I.e.

$$\sum_i^N \Omega_i = \Omega$$

ii Fluxes for the internal surface of a subvolume must be determined by formula(s) involving *other* subvolumes. This constraint ensures the conservative property of the discretized equation. Appropriate internal fluxes should cancel out when the subvolumes and their discretized quantities are added.

For our derivations we will choose two mesh designs. The first one will be a normal cartesian mesh with rectangular cells that are horizontally uniform in every depth layer. The second mesh design will incorporate the partial-cell method where some of the bottom-most cells have their height altered. Both mesh designs are shown in Figure 1.8. The horizontal uniformity of the depth surfaces is lost in a number of depth layers. It will be assumed that the tracked variable (velocity in this case) is defined within the cells. Since finite-volume meshes do not use explicit data points, one can think of the cell's variable as a volume-averaged value of that variable inside the cell.

Cell-face flux determination For Equation 1.8 to be explicitly formulated we need to know how to represent the individual velocity fluxes through each face of a finite volume cell like the one given in Figure 1.9.

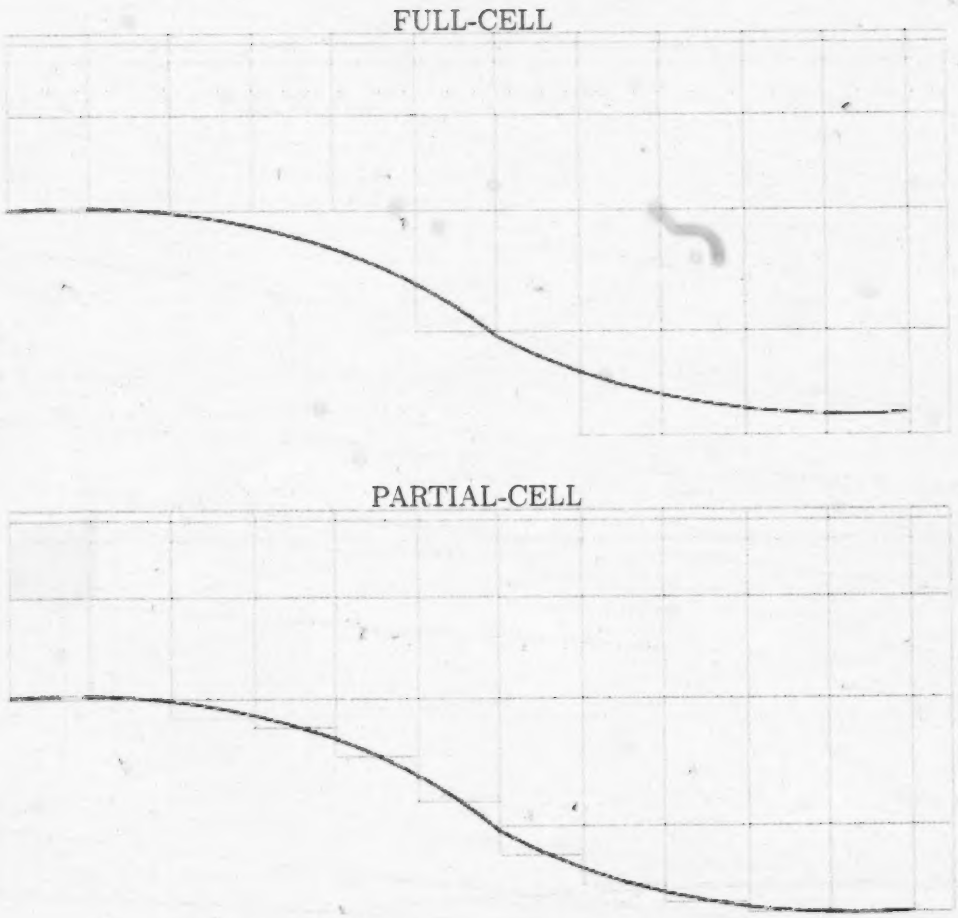

Figure 1.8: Cartesian mesh designs used for our discretization exercise.

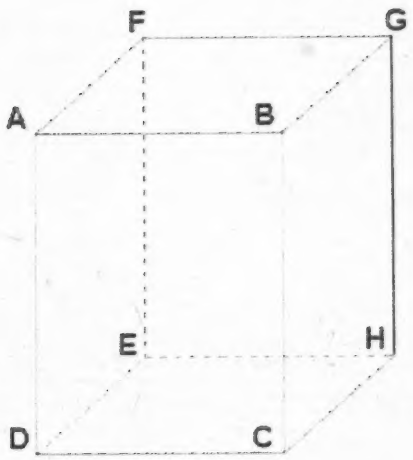

Figure 1.9: Example of a rectangular finite volume cell found in the mesh designs of Figure 1.8.

The grid cell in Figure 1.9 has six faces and thus six velocity fluxes must be accounted for in the discrete equation.

$$\begin{aligned}\sum_{sides} \vec{u} \cdot \vec{S} =& \vec{u}_{BCHG} \cdot \vec{S}_{BCHG} + \vec{u}_{AFED} \cdot \vec{S}_{AFED} + \vec{u}_{ADCB} \cdot \vec{S}_{ADCB} \\ &+ \vec{u}_{EFGH} \cdot \vec{S}_{EFGH} + \vec{u}_{CDEH} \cdot \vec{S}_{CDEH} + \vec{u}_{ABGF} \cdot \vec{S}_{ABGF}\end{aligned} \tag{1.9}$$

We will depict each flux vector $\{\vec{u}_{BCHG}, \vec{u}_{AFED}, \ldots\}$ as the average of the water velocity between two adjacent mesh cells that share a particular cell face. Specifically, the velocity flux vectors are

$$\vec{u}_{BCHG} = \tfrac{1}{2}\left(\vec{u}_{i+1,j,k} + \vec{u}_{ijk}\right) \tag{1.10}$$

$$\vec{u}_{AFED} = \tfrac{1}{2}\left(\vec{u}_{ijk} + \vec{u}_{i-1,j,k}\right) \tag{1.11}$$

$$\vec{u}_{ADCB} = \tfrac{1}{2}\left(\vec{u}_{i,j+1,k} + \vec{u}_{ijk}\right) \tag{1.12}$$

$$\vec{u}_{EFGH} = \tfrac{1}{2}\left(\vec{u}_{ijk} + \vec{u}_{i,j-1,k}\right) \tag{1.13}$$

$$\vec{u}_{CDEH} = \tfrac{1}{2}\left(\vec{u}_{i,j,k+1} + \vec{u}_{ijk}\right) \tag{1.14}$$

$$\vec{u}_{ABGF} = \tfrac{1}{2}\left(\vec{u}_{ijk} + \vec{u}_{i,j,k-1}\right) \tag{1.15}$$

Normal surface vectors Before Equation 1.9 can be evaluated we also need the outward normal surface vectors for each cell face. The outward normal surface vector can be determined for any planar cell face by taking the vector product of its two diagonals. When choosing the diagonal vectors remember that the surface vector must point *out* of the cell and that a right-handed coordinate system is being used. As an example let's calculate the outward normal surface vector for the cell face

ABCD denoted as $\vec{S}_{ABCD}$.

$$\begin{aligned}\vec{S}_{ADCB} &= \frac{1}{2}(\vec{r}_{AC} \times \vec{r}_{BD}) \\ &= \frac{1}{2}\begin{vmatrix} \hat{i} & \hat{j} & \hat{k} \\ \Delta x & 0 & \Delta z_N \\ -\Delta x & 0 & \Delta z_N \end{vmatrix} \\ &= (0, \Delta x \Delta z_N, 0)\end{aligned}$$

where Δz_N is the thickness of the N^{th} depth layer. The above vector product creates a parallelogram with a height of $|\vec{r}_{AC}|$ and a width of $|\vec{r}_{BD}|$. The area of this parallelogram will always be twice that of the surface area of the rectangular cell face. Thus we apply a factor of $\frac{1}{2}$ to the vector product of the body diagonals(Hirsch, 1990).

If rectangular mesh cells are used then the normal surface vectors can be easily determined. The magnitude of each normal surface vector is simply the area of the corresponding cell face. One can also exploit the symmetry of the rectangular mesh cell such that only three normal surface vectors need to be calculated since the following relations hold.

$$\begin{aligned}\vec{S}_{BCHG} &= (\Delta y \Delta z_N, 0, 0) = -\vec{S}_{AFED} \\ \vec{S}_{ADCB} &= (0, \Delta x \Delta z_N, 0) = -\vec{S}_{EFGH} \\ \vec{S}_{CDEH} &= (0, 0, \Delta x \Delta y) = -\vec{S}_{ABGF}\end{aligned} \tag{1.16}$$

Final discrete equation Substituting in the flux vector relations (Equations 1.10-1.15) and the normal surface vectors (Equation 1.16) into Equation 1.9 yields

$$\left(\frac{u_{i+1,j,k} - u_{i-1,j,k}}{2}\right)\Delta y \Delta z_N + \left(\frac{v_{i,j+1,k} - v_{i,j-1,k}}{2}\right)\Delta x \Delta z_N + \left(\frac{w_{i,j,k+1} - w_{i,j,k-1}}{2}\right)\Delta x \Delta y = 0$$

If we divide through by the cell volume, $\Omega = \Delta x \Delta y \Delta z_N$, then we get

$$\left(\frac{u_{i+1,j,k} - u_{i-1,j,k}}{2\Delta x}\right) + \left(\frac{v_{i,j+1,k} - v_{i,j,-1k}}{2\Delta y}\right) + \left(\frac{w_{i,j,k+1} - w_{i,j,k-1}}{2\Delta z_N}\right) = 0 \qquad (1.17)$$

Note that this discrete equation is the same as the equation one would get if a spatially-central finite-difference discretization scheme was applied to Equation 1.7 where Δz is replaced by Δz_N.

1.3.3 Equation of conservation for linear momentum

The conservation of linear momentum equations are an important part of the governing equations for describing ocean circulation in OGCMs. In this section we will derive a simplified version of the integral linear momentum conservation equations for fluid flow. We will then apply the finite-volume discretization scheme on the integral equations.

Derivation Let's assume that we have a fluid parcel of volume $d\Omega$ and constant density ρ that is under the influence of a velocity field $\vec{u}$. The total force on the fluid parcel is the sum of the internal and external forces it is subjected to.

$$f_{TOTAL} = f_{internal} + f_{external}$$

It will be assumed that the only external force the parcel is subjected to is gravity.

$$f_{TOTAL} = f_{internal} + \rho\vec{g}(\,d\Omega)$$

Newton's second law of motion states that the sum of these forces must equal the product of the parcel's mass and its acceleration.

$$\begin{aligned} f_{TOTAL} &= mass \times acceleration \\ f_{internal} + \rho\vec{g}(\,d\Omega) &= (\rho\,d\Omega)\left(\tfrac{\partial\vec{u}}{\partial t} + (\vec{u}+\vec{\nabla})\vec{u}\right) \end{aligned} \tag{1.18}$$

If we assume that the fluid is Newtonian then from Cauchy's equation of motion for continuous media (Acheson, 1990) we find that

$$f_{internal} = \frac{\partial T_{ij}}{\partial x_j} \quad i,j \in \{1,2,3\}$$

where T_{ij} is a symmetric rank-two tensor describing stress forces inside the fluid parcel. Additionally, Acheson (1990) shows that if the fluid is incompressible (i.e. $\nabla \cdot \vec{u} = 0$) then the stress tensor has the following form.

$$T_{ij} = -p\delta_{ij} + \mu\left(\frac{\partial u_j}{\partial x_i} + \frac{\partial u_i}{\partial x_j}\right)$$

μ is called the fluid's molecular viscosity and is considered to be a constant value. Substituting the last relation into Equation 1.18 produces

$$\begin{aligned} (\rho\,d\Omega)\left(\frac{\partial\vec{u}}{\partial t} + (\vec{u}+\vec{\nabla})\vec{u}\right) &= -\tfrac{\partial p}{\partial x_i} + \mu\tfrac{\partial}{\partial x_j}\left(\tfrac{\partial u_j}{\partial x_i} + \tfrac{\partial u_i}{\partial x_j}\right) + \rho g_i \\ &= -\nabla p + \mu\nabla(\underbrace{\nabla\cdot\vec{u}}_{0}) + \mu\nabla^2\vec{u} + \rho\vec{g} \\ &= -\nabla p + \mu\nabla^2\vec{u} + \rho\vec{g} \end{aligned} \tag{1.19}$$

Letting $\vec{u} = (u, v)$, the volume integral equations for horizontal momentum conservation are

$$\frac{\partial}{\partial t}\int_\Omega \rho u \, d\Omega + \int_\Omega \rho(\vec{u}\cdot\nabla u)\, d\Omega = -\int_\Omega \frac{\partial p}{\partial x}\, d\Omega + \int_\Omega \mu\nabla^2 u \, d\Omega \tag{1.20}$$

$$\frac{\partial}{\partial t}\int_\Omega \rho v \, d\Omega + \int_\Omega \rho(\vec{u}\cdot\nabla v)\, d\Omega = -\int_\Omega \frac{\partial p}{\partial y}\, d\Omega + \int_\Omega \mu\nabla^2 v \, d\Omega \tag{1.21}$$

With a bit of manipulation one can rewrite the nonlinear term in Equation 1.20 as

$$\vec{u}\cdot\nabla u = \nabla\cdot(u\vec{u}) - u\underbrace{(\nabla\cdot\vec{u})}_{0}$$

$$= \nabla\cdot(u\vec{u})$$

where our incompressibility assumption for the fluid comes into play again. The same simplification can be applied to the nonlinear term in Equation 1.21

$$\vec{u}\cdot\nabla v = \nabla\cdot(v\vec{u})$$

Gauss' divergence theorem can now be applied to the two corresponding volume integrals.

$$\int_\Omega \rho[\nabla\cdot(u\vec{u})]\, d\Omega = \oint_S \rho u\vec{u}\cdot\vec{dS}$$

$$\int_\Omega \rho[\nabla\cdot(v\vec{u})]\, d\Omega = \oint_S \rho v\vec{u}\cdot\vec{dS}$$

Thus Equations 1.20 and 1.21 can be rewritten as

$$\frac{\partial}{\partial t}\int_\Omega \rho u \, d\Omega + \rho\oint_S u\vec{u}\cdot\vec{dS} = -\int_\Omega p_x \, d\Omega + \mu\oint_S \nabla u\cdot\vec{dS} \tag{1.22}$$

$$\frac{\partial}{\partial t}\int_\Omega \rho v \, d\Omega + \rho\oint_S v\vec{u}\cdot\vec{dS} = -\int_\Omega p_y \, d\Omega + \mu\oint_S \nabla v\cdot\vec{dS} \tag{1.23}$$

Now we want to apply our finite-volume discretization scheme to Equations 1.22 and 1.23. We will use the same mesh that we used for the finite-volume discretization of the continuity equation as shown in Figure 1.8. As a consequence, we do not need to re-determine the normal surface vectors for the cell faces. Also, for the sake of brievity, only the discretization of Equation 1.22 will be explicitly shown and its discretization will be done on a term-by-term basis.

Discretization of time dependent term The time-dependent term is a volume flux term. Thus

$$\frac{\partial}{\partial t}\int_{\Omega} \rho u \, d\Omega = \frac{\partial}{\partial t}\int_{\Omega_i} \rho_i u_i \, d\Omega$$

Only one subvolume is used -the volume of the desired mesh cell, $\Omega_{ijk} = \Delta x \Delta y \Delta z_N$. Here i, j, k are the cartesian indicies representing the cell's location. So, the appropriate discrete equation is

$$\frac{\partial}{\partial t}\left(\rho_{ijk} u_{ijk} \Omega_{ijk}\right) = \frac{\partial}{\partial t}\left(\rho_{ijk} u_{ijk}\right) \Delta x \Delta y \Delta z_N \tag{1.24}$$

Discretization of pressure term Notice that we can apply the divergence theorem on the original pressure volume integral as

$$\int_{\Omega} \nabla p \, d\Omega = \oint_{S} p \, d\vec{S}$$

Here the surface integral can be approximated by the sum of the pressure fluxes across each face of the mesh cell. We again use the averaging technique to numerically depict

the pressure fluxes as so

$$p_{BCHG} = \frac{1}{2}\left(p_{i+1,j,k} + p_{ijk}\right)$$

$$p_{ADEF} = \frac{1}{2}\left(p_{ijk} + p_{i-1,j,k}\right)$$

$$p_{ABCD} = \frac{1}{2}\left(p_{i,j+1,k} + p_{ijk}\right)$$

$$p_{EFGH} = \frac{1}{2}\left(p_{ijk} + p_{i,j-1,k}\right)$$

$$p_{CDEH} = \frac{1}{2}\left(p_{i,j,k+1} + p_{ijk}\right)$$

$$p_{ABGF} = \frac{1}{2}\left(p_{ijk} + p_{i,j,k+1}\right)$$

The surface integral is then discretized in the following way.

$$\oint_S p\,d\vec{S} \approx \sum_{sides} p\vec{S}$$

where

$$\begin{aligned}\sum_{sides} p\vec{S} &= (p_{BCHG} - p_{ADEF})\vec{S}_{BCHG} + (p_{ABCD} - p_{EFGH})\vec{S}_{ABCD} \\ &\quad + (p_{CDEH} - p_{ABGF})\vec{S}_{CDEH} \\ &= \left(\frac{p_{i+1,j,k} - p_{i-1,j,k}}{2}\right)\Delta y \Delta z_N + \left(\frac{p_{i,j+1,k} - p_{i,j-1,k}}{2}\right)\Delta x \Delta z_N \\ &\quad + \left(\frac{p_{i,j,k+1} - p_{i,j,k-1}}{2}\right)\Delta x \Delta y\end{aligned}$$

However, we are only interested in changes in the pressure along the x-coordinate axis (i.e. along the direction of $\vec{S}_{BCHG}$). Therefore the discrete term of interest is

$$\oint_S p_x\,dS \approx \left(\frac{p_{i+1,j,k} - p_{i-1,j,k}}{2}\right)\Delta y \Delta z_N \tag{1.25}$$

Discretization of Laplacian term The next term to be discretized is the viscous term containing a Laplacian operator applied to the velocity vector $\vec{u}$.

$$\nabla^2 \vec{u} = (\nabla^2 u, \nabla^2 v, \nabla^2 w)$$

If we look at only the volume integral of the Laplacian term in the x-coordinate direction then we get

$$\int_{\Omega} \mu \nabla^2 u \, d\Omega = \oint_{S} \mu \vec{\nabla} u \cdot \vec{dS}$$

where we have applied Gauss' divergence theorem on the volume integral. Note that μ is assumed to be a constant real value.

Since the Laplacian term can be rewritten as a surface integral, we can approximate it as the sum of fluxes passing through the six cell faces of our rectangular finite volume cell.

$$\oint_{S} \mu \vec{\nabla} u \cdot \vec{dS} \approx \mu(u_x S_{BCHG} + u_x S_{ADEF} + u_y S_{ABCD} + u_y S_{EFGH} + u_z S_{CDEH} + u_z S_{ABGF})$$

where (u_x, u_y, u_z) are volume-averaged estimates of the spatial derivatives of the horizontal velocity component, u. Using the symmetry found in our finite volume cell we can re-formulate the above relation as

$$\begin{aligned} \oint_{S} \mu \vec{\nabla} u \cdot \vec{dS} \approx & \mu \left(\frac{\partial u}{\partial x}|_{BCHG} - \frac{\partial u}{\partial x}|_{ADEF} \right) S_{BCHG} \\ & + \mu \left(\frac{\partial u}{\partial y}|_{ABCD} - \frac{\partial u}{\partial y}|_{EFGH} \right) S_{ABCD} \\ & + \mu \left(\frac{\partial u}{\partial z}|_{CDEH} - \frac{\partial u}{\partial z}|_{ABGF} \right) S_{CDEH} \end{aligned}$$

The derivative terms are approximated by replacing them with appropriate spatially-forward finite-difference discretizations.

$$\begin{aligned}\oint_S \mu\vec{\nabla}u \cdot d\vec{S} \approx & \mu\left(\frac{u_{i+1,j,k} - 2u_{ijk} + u_{i-1,j,k}}{\Delta x}\right)\Delta y\Delta z_N \\ & + \mu\left(\frac{u_{i,j+1,k} - 2u_{ijk} + u_{i,j-1,k}}{\Delta y}\right)\Delta x\Delta z_N \\ & + \mu\left(\frac{u_{i,j,k+1} - 2u_{ijk} + u_{i,j,k-1}}{\Delta z_N}\right)\Delta x\Delta y\end{aligned} \tag{1.26}$$

Discretization of the nonlinear term As with the other surface integral terms, the nonlinear acceleration term can be approximated by the sum of fluxes through the cell faces.

$$\oint_S \rho u\vec{u} \cdot d\vec{S} \approx \sum_{sides} \rho_{ijk}u_{ijk}\left(\vec{u} \cdot \vec{S}\right)$$

Here we want to numerically describe the flux of the horizontal water velocity, u, across the six cell faces. For this we employ the six velocity flux vectors derived in Equation 1.10.

Substituting these numerical descriptions of the velocity fluxes into the sum equations gives us

$$\begin{aligned}\sum_{sides} \rho_{ijk}u_i\left(\vec{u} \cdot \vec{S}\right) = & \ \rho_{ijk}\left(\tfrac{u_{BCHG}-u_{ADEF}}{2}\right)\vec{u} \cdot \vec{S}_{BCHG} \\ & + \rho_{ijk}\left(\tfrac{u_{ABCD}-u_{EFGH}}{2}\right)\vec{u} \cdot \vec{S}_{ABCD} \\ & + \rho_{ijk}\left(\tfrac{u_{CDEH}-u_{ABGF}}{2}\right)\vec{u} \cdot \vec{S}_{CDEF}\end{aligned}$$

or

$$\begin{aligned}\sum_{sides} \rho_{ijk} u_i \left(\vec{u} \cdot \vec{S}\right) = &\rho_{ijk} u_{ijk} \left(\frac{u_{i+1,j,k} - u_{i-1,j,k}}{2}\right) \Delta y \Delta z_N \\ &+ \rho_{ijk} v_{ijk} \left(\frac{u_{i,j+1,k} - u_{i,j-1,k}}{2}\right) \Delta x \Delta z_N \\ &+ \rho_{ijk} w_{ijk} \left(\frac{u_{i,j,k+1} - u_{i,j,k-1}}{2}\right) \Delta x \Delta y\end{aligned} \tag{1.27}$$

Final discrete equation Gathering the terms derived in Equations 1.24-1.27 yields

$$\begin{aligned}&\frac{\partial}{\partial t}\left(\rho_{ijk} u_{ijk} \Delta x \Delta y \Delta z_N\right) \\ &+\rho_{ijk} u_{ijk} \left(\frac{u_{i+1,j,k} - u_{i-1,j,k}}{2}\right) \Delta y \Delta z_N \\ &+\rho_{ijk} v_{ijk} \left(\frac{u_{i,j+1,k} - u_{i,j-1,k}}{2}\right) \Delta x \Delta z_N \\ &+\rho_{ijk} w_{ijk} \left(\frac{u_{i,j,k+1} - u_{i,j,k-1}}{2}\right) \Delta x \Delta y \\ &= -\left(\frac{p_{i+1,j,k} - p_{i-1,j,k}}{2}\right) \Delta y \Delta z_N \\ &+\mu \left(\frac{u_{i+1,j,k} - 2u_{ijk} + u_{i-1,j,k}}{\Delta x}\right) \Delta y \Delta z_N \\ &+\mu \left(\frac{u_{i,j+1,k} - 2u_{ijk} + u_{i,j-1,k}}{\Delta y}\right) \Delta x \Delta z_N \\ &+\mu \left(\frac{u_{i,j,k+1} - 2u_{ijk} + u_{i,j,k-1}}{\Delta z_N}\right) \Delta x \Delta y\end{aligned}$$

Dividing through by the cell's volume, $\Delta x \Delta y \Delta z_N$, yields

$$\begin{aligned}&\frac{\partial}{\partial t}\left(\rho_{ijk} u_{ijk}\right) + \rho_{ijk} u_{ijk} \left(\frac{u_{i+1,j,k} - u_{i-1,j,k}}{2\Delta x}\right) \\ &+\rho_{ijk} v_{ijk} \left(\frac{u_{i,j+1,k} - u_{i,j-1,k}}{2\Delta y}\right) + \rho_{ijk} w_{ijk} \left(\frac{u_{i,j,k+1} - u_{i,j,k-1}}{2\Delta z_N}\right) \\ &= -\left(\frac{p_{i+1,j,k} - p_{i-1,j,k}}{2\Delta x}\right) + \mu \left(\frac{u_{i+1,j,k} - 2u_{ijk} + u_{i-1,j,k}}{(\Delta x)^2}\right) \\ &+\mu \left(\frac{u_{i,j+1,k} - 2u_{ijk} + u_{i,j-1,k}}{(\Delta y)^2}\right) + \mu \left(\frac{u_{i,j,k+1} - 2u_{ijk} + u_{i,j,k-1}}{(\Delta z_N)^2}\right)\end{aligned} \tag{1.28}$$

Note that one can get the exact same form of Equation 1.28 by directly applying a spatially-centred finite difference discretization scheme on Equation 1.22. A finite-volume discretization of Equation 1.23 would follow the same procedure we just discussed.

1.3.4 Employing partial cells

Discrete equations 1.17 and 1.28 are formed on the assumption that they are discretized onto a uniform cartesian mesh. Suppose one wants to apply the discrete equations to the partial cell mesh given in Figure 1.8. The presence of partial cells in this mesh requires that we modify Equations 1.17 and 1.28 so as to account for the loss of horizontal uniformity in some of the depth surfaces. Fortunately, our decision to use rectangular finite-volume cells simplifies these modifications.

The basis of the finite-volume method is the determination of the flux of a tracked variable across each cell face. A cell face with a larger surface area will have a larger flux of the tracked variable than a cell face with a smaller surface area. Therefore the magnitude of the flux between two adjacent finite volume cells will be limited to the cell with the smaller surface area of the shared cell face boundary. An example of this is shown in Figure (1.10) where we have a full cell adjacent to a partial cell. Assume that the shaded region is a solid boundary where no flux can occur. Both cells will experience a flux between their shared cell face. However, the magnitude of this flux is limited by the surface area of the cell face of the shorter partial cell

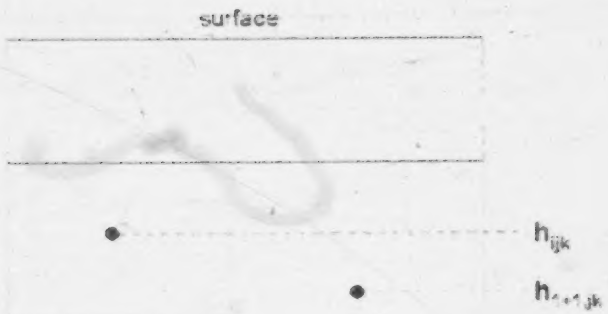

Figure 1.10: Two adjacent finite-volume cells with different cell heights.

regardless of the height of the full cell. I.e., the magnitude of the flux will be $\Delta x \Delta z_N^*$ where Δz_N^* is called the *effective cell height* and defined by the minimum height of the two adjacent cells located in depth layer N.

$$z_N^* = \min\left(\Delta z_{i,k}, \Delta z_{i+1,k}\right)$$

Let's now consider a partial cell residing in a particular depth layer of some three-dimensional mesh. The cell will have up to four other finite volume cells horizontally adjacent to it. Its effective cell height would then be the minimum cell height of those cells. I.e.

$$z_N^* = \min\left(\Delta z_{i+1,j,k}, \Delta z_{i-1,j,k}, \Delta z_{i,j+1,k}, \Delta z_{i,j-1,k}, \Delta z_{i,j,k}\right) \tag{1.29}$$

Vertically or diagonally adjacent cells are not included in the determination of the

effective cell height as they reside in a different depth layer. Notice that for a full-cell mesh or for an interior depth layer with no contact with the topography,

$$z_N^* = z_N$$

It should now be clear why the partial-cell method has gained so much popularity with numerical modelers: to incorporate partial cells into Equations 1.17 and 1.28 all one needs to do is to replace z_N by z_N^*. The only additional significant computational costs arise from the determination of the effective cell heights for the mesh. However, this determination only needs to be done once during an initial sweep of the finite volume mesh.

1.3.5 Discretized hydrostatic primitive equations

Discrete equations 1.17 and 1.28 are very simplified versions of the actual discrete equations used in OGCMs. For example, equation 1.28 does not have any Coriolis or other term to describe effects of the earth's rotation on modelled circulation patterns. The governing equations in most OGCMS are usually discretized onto a spherical coordinate, (λ, ϕ, z), mesh instead of a cartesian mesh. A finite-difference discretization of the hydrostatic primitive equations in spherical coordinates is given in (Haidvogel and Beckmann, 1999). The finite volume discretization of the hydrostatic primitive equations used in MOM are explicitly shown in (Pacanowski and Gnanadesikan, 1998). The procedure for obtaining those discrete equations is exactly the same as the procedure used in the previous section. More importantly, the

adaptation of those discrete equations to meshes employing rectangular partial cells is exactly the same as the discrete equations we derived earlier. All one needs to do is to determine the effective cell height, z_N^*, for each partial cell and insert it into the appropriate discrete equations. Explict formulations of these discrete equations using full-cell and partial-cell meshes are given by Pacanowski and Gnanadesikan (1998).

Modifying an existing z-level OGCM that uses discretized hydrostatic primitive equations to describe ocean circulation is quite simple. The finite-difference and finite-volume meshes will be the same except at the ocean-bottom boundary where partial cells are used in the finite-volume mesh. In the ocean interior, where the depth layers are horizontally uniform, the finite volume discretizations of the primitive equations are exactly the same as the finite-difference discretizations. Therefore, no changes are necessary. Finite volume cells that intersect the ocean-bottom boundary must determine their effective cell heights and use those heights in their interpretation of the discretized equations. Effective cell height determination only needs to be done once and can be done in an initial sweep of the mesh. Note that interior cells have their effective cell height equal to the height of the depth layer, Δz_N. One must also remember that the use of partial cells effects the approximation of water volume in each water column of the finite volume mesh (Adcroft et al., 1997).

1.3.6 Order of accuracy in vertical discretizations

As previously stated, the thicknesses of the depth layers in a z-level model can vary. Usually the depth layer thickness is stretched using some sort of analytical function. When a proper stretching procedure is applied, the finite-difference (and finite-volume) discretizations of the governing equations are second-order accurate when only full cells are used. The use of partial cells breaks the analytical setting of depth thickness in the bottom-most depth layer. As a consequence the bottom depth layer is only first-order accurate (Pacanowski and Gnanadesikan, 1998). However, since the partial-cell method significantly reduces the effects of staircase topography, it is generally assumed that the accuracy loss caused by the partial cells is more than compensated for by the improved topography representation. In other words, it is assumed that a partial-cell model will remain second-order accurate overall because we have a first-order accurate procedure addressing a zeroth-order problem (topography representation)(Treguier et al., 1996).

1.4 Numerical errors introduced by partial-cells

Numerical ocean models tend to assume that horizontal motion in the world ocean's circulation is much larger and thus much more significant to represent than the corresponding vertical motion. Consequencely, they usually solve discretized versions of the horizontal Navier-Stokes equations only. Vertical pressure gradients are estimated using a hydrostatic pressure approximation which remains valid in the case

of horizontally-uniform depth layers. The application of partial cells can lead to horizontal nonuniformity in the bottommost depth layer(s) leading to a situation similiar to the on depicted in Figure 1.10. In this case, the height between two adjacent partial cells may be quite large thereby invalidating the hydrostatic pressure assumption. To investigate this situation further, we will briefly describe a pressure correction procedure outlined by Pacanowski and Gnanadesikan (1998). Let P be the true pressure in a particular depth layer which can be written as the sum of the hydrostatic pressure at the layer's depth ($\mathbf{P}$) and a correction pressure (P_{corr}).

$$P \equiv \mathbf{P} + P_{corr}$$

P_{corr} corrects for any horizontal non-uniformity in the depth layer. Applying the appropriate integral definitions yields

$$P \equiv g \int_z^{\eta} \rho \, dz + g \int_{\Delta s} \rho \, dz$$

where η is the free surface of the ocean domain and Δs is the vertical fluctuations in the depth layer. In a full-cell model, $\Delta s = 0$ (all depth layers are horizontally uniform) while in a corresponding partial-cell model Δs can be nonzero in the bottommost depth layers.

$$g \left[\int_z^{\eta} \rho \, dz + \rho(z_N) \Delta s \right]$$

where $\rho(z_N)$ is the in-situ density computed at the depth of the N_{th} depth surface. The spatial derivative terms involving pressure in the horizontal Navier-Stokes equations

become

$$-\frac{\partial P}{\partial x} \approx -g\left[\frac{\partial}{\partial x}\left(\int_z^\eta \rho\, dz\right) + \rho(z_N)\frac{\partial \Delta s}{\partial x}\right]$$
$$\frac{\partial P}{\partial y} \approx g\left[\frac{\partial}{\partial y}\left(\int_z^\eta \rho\, dz\right) + \rho(z_N)\frac{\partial \Delta s}{\partial y}\right] \tag{1.30}$$

In Equation 1.30 we are trying to compensate for any significant breakdown in the hydrostatic pressure assumption without resorting to a numerical solution of the vertical Navier-Stokes equation (which would lead to a significant increase in computational costs). Theoretically, it is only required for the correction factor to be applied to the bottommost depth layer(s) as the interior depth layers retain their horizontal uniformity ($\Delta s = 0$). However, in practice, there tends to be some interaction between the interior and bottommost depth layers in a discrete numerical system thus the use of approximate equalities in Equation 1.30. These false horizontal pressure gradients do give rise to unphysical water velocities and mixing. Fortunately, the magnitude of these inaccuracies are smaller than the first-order improvement in topographic representation produced by partial-cells. Further details of this pressure correction procedure are given by Treguier and Bryan (1996) including a full derivation involving partial-cell and other non-uniform meshes.

Chapter 2

The JEBAR Term

2.1 JEBAR's origins

Sverdrup's balance between wind stress and Coriolis forcing produces a reasonable description of the current structure of the subtropical Atlantic. However current velocities in the Gulf Stream tended to be an order of magnitude smaller than observed quantities. Sarkisyan and Ivanov (1971) determined that when realistic topography and density stratification are include in the depth-integrated transport calculations the corresponding Gulf Stream current velocities were increased by the necessary order of magnitude. A similar determination was made by Holland and Hirschman (1972) using a coarse 1^o prognostic model of the North Atlantic. They conducted a series numerical experiments with each one focusing on the effect of one specific parameter on the computed maximum Gulf Stream transport. Using the traditional Sverdrup balance on a homogeneous domain with a flat-bottomed topography the maximum computed transport was 14 Sv. That value doubled when density stratification was

added. With both realistic topography and stratification present, the model predicted a maximum transport value of 81 Sv which is much closer to observed maxima. Holland and Hirschmann attributed the increased transport to an "ocean-bottom torque" that explicitly appeared in the vorticity balance of the barotropic flow.

Let's now derive this torque term described by Holland and Hirschman (1972). We start with the vector representation of the Navier-Stokes equations employed in MOMA(Udall, 1996).

$$\underbrace{\frac{\partial \vec{u}}{\partial t} + \vec{u}\cdot\nabla\vec{u} + w\frac{\partial \vec{u}}{\partial z}}_{\text{Advection}} + \underbrace{f\hat{k}\times\vec{u}}_{\text{Coriolis}} = \underbrace{-\frac{1}{\rho_o}\vec{\nabla}p}_{\text{Pressure}} + \underbrace{\vec{\nabla}\cdot(\kappa\nabla\vec{u})}_{\text{Diffusion}} + \underbrace{\vec{\tau}}_{\text{Stress}} \tag{2.1}$$

Variable	Definition
$\vec{u}$	horizontal current velocities (u, v)
w	vertical current velocity
ρ_o	reference density for seawater$\left(1025.25\frac{kg}{m^3}\right)$
p	in-situ pressure
κ	horizontal diffusion coefficient
$\vec{u}_{bot}$	ocean-bottom horizontal current velocities(u_{bot}, v_{bot})
$\vec{u}_{free}$	free-surface horizontal current velocities(u_{free}, v_{free})
$\vec{\tau}$	external stress (wind and friction)
H	ocean-bottom topography
η	free sea surface
ϕ	latitude
Ω	rate of rotation for the Earth $(7.29212\times10^{-5}s^{-1})$

f is the Coriolis parameter and is determined by the relation $f = 2\Omega\sin\phi$. The diffusion terms in Equation 2.1 represent eddy transport not resolved by the nonlinear advection terms (Udall, 1996). κ is a kinematic viscosity term whose value can be altered according to the grid spacing employed.

A term grouping scheme is applied where Equation 2.1is broken into five groups of terms. A cartesian coordinate system is assumed for the sake of simplicity. (A

derivation for a spherical coordinate system is given in Appendix One.)

The governing vector equation of the barotropic flow is formed by depth-averaging the Navier-Stokes equations.

$$\frac{\partial \vec{U}}{\partial t} - \frac{\vec{u}_{free}}{\eta + H}\frac{\partial \eta}{\partial t} + f\hat{k} \times \vec{U} = -\frac{1}{\rho_o}\vec{\nabla}P + \frac{\left(p_{free}\vec{\nabla}\eta - p_{bot}\vec{\nabla}H\right)}{\rho_o(\eta + H)} + \frac{\vec{\tau}}{\eta + H} + \vec{G} \quad (2.2)$$

where $\vec{U}$ is defined as the depth-averaged current velocity

$$\vec{U} = (U, V) = \frac{1}{\eta + H}\int_H^\eta \vec{u}\, dz$$

$\vec{u}_{free}$ and $\vec{u}_{bot}$ are the free surface and ocean bottom current velocities. P, p_{free} and p_{bot} are the depth-integrated, free-surface and ocean-bottom pressures respectively. The three pressure terms arise from Leibnitz's rule for integration (Jeffrey, 1995) where for the x-component

$$\frac{\partial P}{\partial x} = p_{free}\frac{\partial \eta}{\partial x} - p_{bot}\frac{\partial H}{\partial x} + \int_H^\eta \left(\frac{\partial p}{\partial x}\right) dz$$

Similarly, the extra temporal term appears from

$$\frac{\partial U}{\partial t} = u_{free}\frac{\partial \eta}{\partial t} + \int_H^\eta \left(\frac{\partial u}{\partial t}\right) dz$$

Liebnitz's rule only generates one additional temporal term since the bottom topography, H, has no temporal variance. The scalar factor $\frac{1}{\eta+H}$ in Equation 2.2 comes from the depth-averaging process over the water column. We define $\vec{G}$ as the sum of the depth-averaged non-linear advection term $\vec{u}\cdot\nabla\vec{u}$ and the depth-averaged Diffusion term written in Equation 2.1.

The vertical component of the curl of Equation 2.2 creates a vorticity equation whose form is similar to that used by Ivanov and Sarkisyan (1971) and Holland (1973).

$$\frac{\partial^2 V}{\partial t \partial x} - \frac{\partial^2 U}{\partial t \partial y} - \frac{1}{\eta + H}\left[\frac{\partial \eta}{\partial t}\left(\frac{\partial v_{free}}{\partial x} - \frac{\partial u_{free}}{\partial y}\right) + v_{free}\frac{\partial^2 \eta}{\partial t \partial x} - u_{free}\frac{\partial^2 \eta}{\partial t \partial y}\right]$$
$$+ f\left(\frac{\partial U}{\partial x} + \frac{\partial V}{\partial y}\right) + V\frac{\partial f}{\partial y} = -\frac{1}{\rho_o}\left[J(\eta, p_{free}) - J(H, p_{bot})\right] + \frac{1}{\eta + H}\left(\frac{\partial \tau^y}{\partial x} - \frac{\partial \tau^x}{\partial y}\right)$$
$$+ \frac{\partial G^y}{\partial x} - \frac{\partial G^x}{\partial y} \tag{2.3}$$

where $J(A, B)$ is the jacobian operator and is defined as

$$J(A, B) = \frac{\partial A}{\partial x}\frac{\partial B}{\partial y} - \frac{\partial A}{\partial y}\frac{\partial B}{\partial x}$$

This jacobian term is the ocean-bottom torque described by Holland and Hirschmann (1972) and it plays a significant role in balancing Equation 2.3. Using a simplistic rectangular oceanic domain with a sloping bottom, Simon (1979) showed that the overall balance in the vorticity equatioin of the depth-integrated flowis achieved mostly between the topographic (ocean-bottom torque) and planetary vorticity terms. In western boundary current regions where current intensification occurred, a kinematic diffusion viscosity term helped maintain the overall vorticity balance. For eastern boundary regions, Simon surmised that the vorticity balance was comprised mostly between the planetary vorticity and wind stress curl terms.

When utilized in diagnostic transport calculations for the North Atlantic, the jacobian term has allowed more accurate predicted transport values. In 1972 Holland and Hirschman(Holland and Hirschman, 1972) conducted a series of numerical experiments where baroclinicity and topographic steering appeared as key compo-

nents in calculating a more accurate approximation of the Gulf Stream transport. Interestingly, they found that neither density stratification nor realistic topographic representation alone contributed to a significant increase in the computed transport value. However when the two effects were combined (as in the jacobian term) there was a relatively large increase in the approximated transport value. Their results coincided with the work performed by Sarkisyan and Ivanov (1971) who found that the inclusion of the jacobian term resulted in an order of magnitude increase in the predicted transport values for the North Atlantic. They originally referred to the term as the Joint Effect of Baroclinicity and Bottom Relief (JEBBR). The acronym was later changed to JEBAR.

2.2 JEBAR applications

The first application of JEBAR was to aid in the determiniation of more accurate transport values in predictive models. Predominantly, this has meant that it be used as a diagnostic tool -using observed or predetermined values for density and topography to compute the appropriate jacobian term. JEBAR has been utilized in the determination of western boundary current transport in the sub-polar gyre(Holland and Hirschman, 1972; Greatbatch et al., 1991), the sub-tropical gyre(Holland, 1973; Simons, 1979), the southern ocean(Rattray Jr., 1982; Hughes and de Cuevas, 2001), and the western sub-tropical Pacific(Bell, 1997).

The addition of JEBAR to diagnostic transport calculations has also led to the

prediction of realistic ocean circulation patterns. Sarkisyan and Ivanov (1971) found that the introduction of realistic topography to their numerical simulation led to the development of a predicted recirculation gyre in the North Atlantic Bight which was later observationally verified. Since JEBAR is the composition of two effects (density stratification and topographic steering), investigations have been conducted to ascertain which effect is more significant in producing accurate predicted transport and current velocity values for the Gulf Stream. Both Greatbatch et al. (1991) and Myers et al. (1996) have demonstrated that ocean-bottom torque in the Irminger Sea makes a significant contribution to observed Gulf Stream and subpolar gyre transports.

JEBAR has also been utilized to describe more localized phenomena. It has been suggested that JEBAR could be the driving mechanism behind slope currents observed in the Celtic Sea(Huthnance, 1984). Sarkisyan and Ivanov (1971) mentioned the possibility of eastern boundary current intensification caused by JEBAR during their initial investigation.

2.3 Describing JEBAR

JEBAR is a difficult concept to visualize. It is not a physical quantity that can be measured but a combination of several physical phenomena. Most studies involving JEBAR utilize it as a diagnostic tool -applying prescribed density, pressure and/or current information to the appropriate JEBAR calculations. For example, Myers (1996) performed a diagnostic investigation which found that JEBAR values in three

key geographical regions are significant in diagnostically calculating a correct Gulf Stream volume transport and pathway.

2.3.1 JEBAR as a vorticity correction

JEBAR is usually represented as the jacobian term $J(H, p_{bot})$ appearing in the vorticity equation of the barotropic flow. Because of this, JEBAR has become known as a correction term that helps maintain an overall vorticity balance in an oceanic domain. However, when one derives the barotropic vorticity equation for the same domain there is no explicit JEBAR term (i.e. no jacobian operator). We can quickly verify this by first looking at the vertical component of the curl of Equation 2.1.

$$\frac{\partial^2 v}{\partial t \partial x} - \frac{\partial^2 u}{\partial t \partial y} + w\left(\frac{\partial^2 v}{\partial z \partial x} - \frac{\partial^2 u}{\partial z \partial y}\right) + f\left(\frac{\partial u}{\partial x} + \frac{\partial v}{\partial y}\right) + \beta v = \tau_x^y - \tau_y^x + I \qquad (2.4)$$

where I is the vertical component of the curl of the non-linear advection and diffusion terms.

Depth-averaging Equation 2.4 yields

$$\text{Advection} + \text{Coriolis} = \text{Stress} + \vec{G} \qquad (2.5)$$

where

$$\text{Advection} \equiv \frac{\partial^2 V}{\partial t \partial x} - \frac{\partial^2 U}{\partial t \partial y} - \frac{1}{\eta + H}\left[v_{free}\frac{\partial^2 \eta}{\partial t \partial x} - u_{free}\frac{\partial^2 \eta}{\partial t \partial y} + \frac{\partial \eta}{\partial t}\left(\frac{\partial v_{free}}{\partial x} - \frac{\partial u_{free}}{\partial y}\right)\right]$$
$$- \frac{1}{\eta + H}\left[\frac{\partial \eta}{\partial x}\frac{\partial v_{free}}{\partial t} - \frac{\partial \eta}{\partial y}\frac{\partial u_{free}}{\partial t} - \frac{\partial H}{\partial x}\frac{\partial v_{bot}}{\partial t} + \frac{\partial H}{\partial y}\frac{\partial u_{bot}}{\partial t}\right]$$

$$\text{Coriolis} \equiv \beta V + f\left[\frac{\partial U}{\partial x} + \frac{\partial V}{\partial y}\right] - \frac{f}{\eta + H}\left[u_{free}\frac{\partial \eta}{\partial x} + v_{free}\frac{\partial \eta}{\partial y} - u_{bot}\frac{\partial H}{\partial x} - v_{bot}\frac{\partial H}{\partial y}\right]$$

$$\text{Stress} \equiv \frac{\partial \tau^y}{\partial x} + \frac{\partial \tau^x}{\partial y}$$

It is assumed that both the nonlinear advection and diffusion terms will be continuous across the entire modelled domain. Therefore, the curl and depth-averaging processes should yield the same result no matter their order of application. Therefore $\vec{G}$ will have the same form as in Equation 2.3.

Subtracting Equation 2.5 from Equation 2.3 gives us a final vorticity correction relation.

$$\frac{\eta + H}{\rho_o}\left[J(\eta, p_{free}) - J(H, p_{bot})\right] = \left[-\frac{\partial \eta}{\partial x}\frac{\partial v_{free}}{\partial t} + \frac{\partial H}{\partial x}\frac{\partial v_{bot}}{\partial t} + \frac{\partial \eta}{\partial t}\frac{\partial u_{free}}{\partial y} - \frac{\partial H}{\partial y}\frac{\partial u_{bot}}{\partial t}\right] + f\left[-u_{free}\frac{\partial \eta}{\partial x} - v_{free}\frac{\partial \eta}{\partial y} + u_{bot}\frac{\partial H}{\partial x} + v_{bot}\frac{\partial H}{\partial y}\right] \quad (2.6)$$

If we ignore the terms involving free surface variations (since they will be small) then one can readily see a relation between the familiar jacobian term and the remaining ocean-bottom current terms.

$$-\frac{H}{\rho_o}\left[J(H, p_{bot})\right] \approx \frac{\partial H}{\partial x}\frac{\partial v_{bot}}{\partial t} - \frac{\partial H}{\partial y}\frac{\partial u_{bot}}{\partial t} + f\left[u_{bot}\frac{\partial H}{\partial x} + v_{bot}\frac{\partial H}{\partial y}\right]$$

Mertz and Wright (1992) were the first to explore this relationship. They refer to the collection of ocean-bottom current terms as the implicit formulation of JEBAR. Notice that with the Coriolis term present, the JEBAR expression gains greater magnitudes at higher latitudes, which has been both predicted and observed. Equation 2.6 also allows an additional physical intepretation of JEBAR as an artificial momentum sink/source(Haidvogel and Beckmann, 1999).

2.3.2 Decomposing JEBAR

We previously stated that JEBAR is the combination of two effects: topographic steering and compensation due to density stratification. Much work has been done to create individual mathematical descriptions for each effect including Greatbatch et al (1991), Mertz and Wright (1992), Myers and Weaver (1996). We will now illustrate the decomposition performed by Greatbatch et al (1991) with the addition of a free surface.

We start by writing the hydrostatic approximation for the perturbation pressure(p) at some depth, z.

$$\frac{\partial p}{\partial z} = -\underbrace{g(\rho - \rho_{hor})}_{b}$$

where ρ is the in-situ density determined at the specific location, b is the buoyancy, and ρ_{hor} is the horizontally-averaged density for the appropriate depth layer. Integrating this relation from some arbitrary depth, z, down to the ocean-bottom surface, H, yields

$$p(z) - p_{bot} = -\int_{-H}^{z} b\, dz \tag{2.7}$$

Depth-integrating Equation 2.7 from the free surface, η, down to the ocean-bottom, H, gives us the following relation.

$$\begin{aligned} (\eta + H)\,[\bar{p} - p_{bot}] &= -\int_{-H}^{\eta}\int_{-H}^{z} b\, dz\, dz' \\ &= -\int_{-H}^{\eta} b(\eta - z)\, dz \end{aligned} \tag{2.8}$$

where $\bar{p}$ is the depth-averaged pressure in the appropriate water column. If we apply the jacobian operator to Equation 2.8 with respect to the topography then we get

$$(\eta + H)\,[J(p_{bot}, H) - J(\bar{p}, H)] = J(\chi, H) \tag{2.9}$$

where we have defined

$$\chi \equiv \int_{-H}^{\eta} b(\eta - z)\, dz$$

as the depth-integrated horizontal pressure perturbation for all depths from the free surface to the ocean bottom.

Equation 2.9 is very similiar to the JEBAR decomposition derived by Greatbatch et al (1991) although our derivation contains a (numerically) small correction factor attributed to the free surface, $b\eta$. $J(\chi, H)$ is the "whole" JEBAR expression that explicitly uses the perturbations in pressure in its computation. $J(p_{bot}, H)$ is the topographic steering component of JEBAR and is commonly referred to as the ocean-bottom torque. $J(\bar{p}, H)$ is the compensation due to density stratification component of JEBAR.

In our previous discussion about JEBAR's importance in maintaining a vorticity balance $J(\chi, H)$ is not explicitly seen. In the vorticity equation of the depth-integrated flow the ocean-bottom torque is explicitly formed but there is no density stratification component of JEBAR present. On the other hand, neither the ocean-bottom torque nor the compensation jacobian is present in the barotropic vorticity equation. What is going on here?

In the depth-integrated flow, the interior density/pressure fluctuations are implicitly applied in the overall current flow structure. The oceanic domain is essentially treated as a homogeneous domain and thus interior vorticity will be neglected. As a result, vorticity arising from the external boundaries (free surface and topography) must have a dominant presence in the vorticity equation for the depth-integrated flow. Therefore the ocean-bottom torque is explicitly present and the compensation jacobian is implicitly present inside the depth-integrated values.

One can think of the barotropic vorticity equation as a vertical averaging of the vorticity arising in each modelled depth layer. JEBAR plays no effect on the vorticity of interior depth layers. However, in depth layers containing bottommost grid cells both topographic steering and density stratification compensation must be accounted for. In these layers ocean-bottom pressure and current velocity must be present. When the vertical "vorticity averaging" is performed one finds a collection of ocean-bottom current velocity and topographic gradient terms in the resulting barotropic vorticity equation. Both topographic steering and density stratification compensation effects are included in the determination of these terms. Therefore, the final vorticity equation does not need to have explicit terms for topographic steering and density stratification compensation- they are already implicitly present.

2.3.3 Summary

We have outlined several different possible physical and mathematical descriptions of JEBAR. The many different ideas and uses of the concept can sometimes blur its actual effect. JEBAR is a diagnostic tool that must use existing pressure or bottom current velocity data and topography. It is a collection of two elements that effect the barotropic flow: the presence of variable topography and density stratification combined with topography variations.

Topography variation is the easier part to visualize and understand in JEBAR. Seamounts, rises, thoughs and steeply dropping continental shelves must obviously effect ocean circulation in some sort of "steering" fashion. The ocean-bottom induced torque on the barotropic flow is represented by

$$J(p_{bot}, H) \equiv \left(\vec{\nabla} \times (p_{bot} \nabla \vec{H})\right) \cdot \hat{k}$$

which is an explicit term in the vorticity equation of the depth-integrated flow. This torque is independent of the wind stress curl and is extremely important in determining deep current and transport patterns(Holland and Hirschman, 1972). Since this component of JEBAR relies directly on topographic representation, an improvement in topographic representations should led to a corresponding improvement in the depiction of this component.

The second component of JEBAR is known as a density stratification compensation effect (Greatbatch et al., 1991). Internal stratification of a flow produces a

pressure gradient that can interact with the topography. This leads to an additional input of vorticity of torque into the flow. The presence of partial cells can lead to potential situations where a hydrostatic pressure approximation is invalid thereby effecting the accuracy of the computed JEBAR effect. Fortunately, the numerical error produced by the invalidation can be corrected for. It is generally accepted that any remaining numerical error is outweighted by the improved accuracy in the representation of the topographic features and individal water column depths.

Chapter 3

Design of experiments

Our goal is to determine differences, if any, in the calculated vorticity balance in the subpolar North Atlantic using the full and partial-cell topographic representations. Two numerical experiments are conducted using the Sub-Polar Ocean Model (SPOM) devised by Myers (2002). In the first experiment, which we call Experiment A, we employ modelled data (current velocities, tracer concentrations, etc) produced by Myers (2002) for fourty years of integration using full-cell topography that has been averaged over the last year of integration. The various terms for the barotropic vorticity equation and vorticity equation for the depth-averaged flow are then computed. In the second experiment, called Experiment B, we determine the same vorticity terms using output generated by Myers (2002) for a partial-cell implementation of SPOM. Modelled data averaged over one month and one decade of integration was also used in the investigation of the two vorticity balances however they did not reveal any significant differences from when the annually averaged data

was utilized.

We devote the rest of this chapter to the description of SPOM, the various settings employed by Myers (2002), and its advantages over other existing models of the subpolar North Atlantic such as the regional configuration of the MIT z-coordinate ocean model by Käse et al (2001).

3.1 SPOM settings

3.1.1 Background

SPOM is a regional configuration of the Modular Ocean Model-Array (MOMA)(Udall, 1996) whose original design stems from the inviscid free-surface ocean model developed by Killworth et al (1991).

MOMA is essentially the same as the Modular Ocean Model (MOM)(Pacanowski and Griffies, 2000) with the major difference between the two models being how variables are stored. Traditionally, variables were stored in a slab-like fashion in MOM, thereby allowing easier swapping of variables between main memory(RAM) and secondary memory devices (hard disks, tape drives, etc). Today computers contain much larger main memory capacities therefore negating the advantages of the slab technique. MOMA stores all active variables in main memory limiting the amount of swapping between the main and secondary memories which is a relatively slow process. This technique is done mostly to ease program faciliation.

MOMA (and therefore SPOM) utilizes a finite-difference solution of the following governing equations.

$$\frac{\partial \vec{u}}{\partial t} + \vec{u} \cdot \nabla \vec{u} + w\frac{\partial \vec{u}}{\partial z} + \vec{f} \times \vec{u} + \frac{1}{\rho_o}\nabla p + \vec{D}_u + \vec{F}_u = 0 \tag{3.1}$$

$$\frac{\partial \vec{T}}{\partial t} + \vec{u} \cdot \nabla \vec{T} + w\frac{\partial \vec{T}}{\partial z} + \vec{D}_T + \vec{F}_T = 0 \tag{3.2}$$

$$\nabla \cdot \vec{u} + \frac{\partial w}{\partial z} = 0 \tag{3.3}$$

$$\frac{\partial p}{\partial z} + \rho g = 0 \tag{3.4}$$

$$\rho = \rho(\Omega, S, p_o) \tag{3.5}$$

Equation 3.1 is a simplified version of the Navier-Stokes equations with $\vec{u}$ being the horizontal velocity, w being the vertical velocity, f being the Coriolis parameter, p being the pressure field, and ρ_o being the reference density for seawater. $\vec{D}_u$ are kinematic diffusion terms representing eddy transport not resolved by the nonlinear advection terms $\vec{u} \cdot \nabla \vec{u}$. In the ocean model the diffusion terms

$$\vec{D}_u = \left(A_h \nabla^4 \vec{u}, A_v \frac{\partial w}{\partial z} \right)$$

where the horizontal diffusion term is represented using a biharmonic mixing scheme that is employed over a small horizontal domain. The vertical diffusion term is applied over a much larger area therefore we have a large difference in the value of the horizontal and vertical viscosity coefficients ($A_h = 7.5 \times 10^{18} \frac{cm^4}{s}, A_v = 1.5 \frac{cm^2}{s}$). These modelled diffusion terms create a viscous effect that is much greater than what is observed in the real world. However, their unphysical magnitudes are required to remain a balance in the kinetic energy of the ocean model.

$\vec{F}_u$ are the external forcing terms arising from surface wind stress and ocean bottom friction. The wind stress is externally set by a climatology created by Trenberth et al (1990). The bottom friction is computed using

$$c_D \vec{u} |\vec{u}|$$

where $\vec{u}$ is the current velocity along the ocean bottom and c_D is a nondimensional drag coefficient chosen to have a value of 10^{-2}.

Equation 3.2 controls the advection and diffusion of the tracer quantities (temperature and salinity) with $\vec{T}$ being the tracer concentration. The tracer diffusion terms, $\vec{D}_T$, have the same form as the momentum diffusion terms with the horizontal and vertical diffusion coefficients being $7.5 \times 10^{18} \frac{cm^4}{s}$ and $0.3 \frac{cm^2}{s}$ respectively. The forcing terms, $\vec{F}_T$, are derived from the heat and freshwater fluxes applied to the free surface. More details about the forcing terms and the vertical mixing scheme can be found in the MOMA manual (Udall, 1996).

Equation 3.3 is the continuity equation and is required for the determination of the vertical velocity (w). The hydrostatic pressure equation is given in Equation 3.4 and requires an in-situ density field, ρ, that is calculated from an equation of state shown in Equation 3.5. Both MOMA and SPOM use an equation of state that is a third order polynomial approximation of the UNESCO equation of state for seawater. The approximation is outlined by Gill (1982).

SPOM utilizes different timesteps for the computation of the barotropic and baroclinic modes. Myers (2002) used an one hour timestep for the baroclinic mode and a

sixty second timestep for the faster evolving barotropic mode and free surface field.

3.1.2 Modelled domain

The North Atlantic sub-polar gyre is of global significance since it contains the deep water formation sites in the Labrador and Greenland Seas. At these sites poleward flowing warm and fresh surface waters are converted to southward flowing cold and salty deeper waters. This deep (water) circulation is an integral part of the thermohaline circulation pattern that redistributes heat and salts throughout the world ocean. Understanding the various current and tracer dynamics in the sub-polar gyre will undoubtedly bring one closer to understanding the complicated convection and water dispersal processes. Many extensive and significant modeling studies of the North Atlantic have been undertaken with some recent examples including Treguier (2001), Käse et al (2001) and Myers (2002).

SPOM's modelled domain extends zonally $0 - 68^o$ West and meridionally $38 - 70^o$ North. The domain contains the entire sub-polar gyre including the Gulf of St Lawrence and the Newfoundland Basin. It also includes the mouth of Hudson's Strait, the southern part of Baffin Bay and a limited region of the Nordic Seas (all of which are important sources of freshwater input). The southern latitude limit nearly coincides with the line of zero wind stress curl across the North Atlantic(Myers, 2002).

SPOM employs a stretched finite-difference grid in the discretization of the governing equations of the model. The horizontal resolution is kept uniform at $\frac{1}{3}^o$ while

the vertical coordinate is divided into thirty-six depth layers of varying thickness. Shallower depth layers are used near the surface to increase resolution of the important mixed surface layer. Layer depth is determined using a scaled vertical coordinate where the most shallow depth layer is 20 meters and the deepest is over 250 meters.

Ocean-bottom topography data is taken from the ETOPO5 dataset(NOAA, 1988) which has a horizontal resolution of $\frac{1}{12}^o$. The data is smoothed to a horizontal resolution of $\frac{1}{3}^o$. In the full-cell model, the heights of the bottommost grid cells are adjusted so that they lie at the nearest depth layer. In the partial-cell model, grid cells containing less than ten meters of water are considered to be land-filled, otherwise the interpolated depths remain unaltered.

3.1.3 Boundary conditions

Along coastlines and ocean bottom

Current velocities, normal momentum fluxes, and normal tracer advective fluxes are set to be zero along the coastlines. Tracer diffusive fluxes are only set to zero when the cell face they act upon is blocked by an adjacent land-filled grid cell.

Horizontal momentum advective fluxes are set to be zero along the ocean bottom. Vertical momentum advective flux is related to the stress created by the vicous drag along the ocean floor. SPOM models this drag force as

$$c_D u_{bot} |\vec{u}_{bot}|$$

where c_D is a dimensionless drag coefficient set to 0.01, and $\vec{u}_{bot}$ is the ocean-bottom current velocity with a magnitude of u_{bot}. Both horizontal and vertical tracer diffusive fluxes are zero along the ocean bottom.

Along free surface

SPOM utilizes the 1^o wind stress climatology created by Trenberth et al (1990). Myers (2002) interpolated the climatological stress values to a horizontal resolution of $\frac{1}{3}^o$. Temperature and salinity values are relaxed to monthly values taken from the NODC data set (1994) using a two hour timescale and a perpetual year format. Additional details about tracer and momentum advection/diffusion at the free surface are given by Myers (2002) and Udall (1996).

Southern open boundary

SPOM utilizes the open boundary scheme by Stevens (1990) along the modelled domain's southern latitude limit. At the boundary baroclinic velocities are computed using linearized versions of the governing equations. Tracers that are advected or diffused out of the modelled domain are allowed to pass only perpendicularly through the open boundary. Advective current velocity flowing out of domain through the open boundary is corrected using a prescribed correcting phase speed

$$\frac{\partial T}{\partial t} + \frac{v + v_{corr}}{a}\frac{\partial T}{\partial \phi} = -K_h \nabla^4 T + K_v \frac{\partial^2 T}{\partial z^2}$$

where the correcting phase speed, v_{corr}, is determined using

$$\frac{\partial T}{\partial t} = -\frac{v_{corr}}{a}\frac{\partial T}{\partial \phi}$$

and T is the corresponding tracer being advected out of the domain. For incoming current velocities, the tracer being advected into the modelled domain is restored to a prescribed value, T_{pre}, via

$$\frac{\partial T}{\partial t} = \frac{T_{pre} - T}{\alpha}$$

where α is the timescale using for the restoration which is chosen to be 25 days. The prescribed tracer data is drawn from Grey and Haines (1999) climatology.

Free surface height must also be restored along the southern open boundary. To do so, Myers (2002) uses a ten grid cell wide "restoration zone" along the southern boundary where the computed free surface height, $\hat{h}_o$, is gradually relaxed to a reference value, $\tilde{h}_o$ using the following formula.

$$h_o = \alpha_i \hat{h}_o + (1 - \alpha_i)\tilde{h}_o$$

where h_o is the free surface height used in the model and α is a relaxation parameter determined by

$$\alpha_i = \left(\frac{N - i + 1}{N}\right)^2$$

N is the number of grid cells over which the restoration process occurs (10 in the case of SPOM) and i is a counter indicating the current grid cell row of the restoration

zone. The reference free surface height values are those computed by a diagnostic finite element ocean model(Myers and Weaver, 1995) at the southern 38° latitude limit.

To help prevent any instability in the restorations processes, modelled topography along the southern open boundary is modified to eliminate southward facing slopes(Pacanowski and Griffies, 2000).

Buffer zones

Open boundary conditions are not employed in Baffin Bay, Hudson Strait, or the Nordic Seas due to a lack of data for those regions. Instead, restoration buffer zones are constructed in each region similar to the free surface restoration zone used along the southern open boundary with the exception that the restoration is applied to all depths in the modelled water column. Each buffer zone is ten grid cells wide and a relaxation parameter is used where its value exponentially decays over the last five grid cells of each buffer zone. All hydrographic properties (current velocities, tracer concentrations, free surface height, etc.) are relaxed to observed values found in the NODC data set (1994) using a one day timescale.

3.1.4 A comment about depth-averaging

Representing the two vorticity equations of interest requires that various terms be depth-averaged. For our investigations all depth-averaged variables are computed

using a weighted sum approach. For example, the depth-averaged current velocity is computed as

$$\vec{U} = \sum_{i=1}^{N} \left(\frac{\Delta z_i}{H} \right) \vec{u}$$

where N is the number of depth layers that the water column intersects. Δz_i is the thickness of the i^{th} depth layer. $\frac{\Delta z_i}{H}$ are the appropriate weight factors used in our depth-averaging approximation process. This choice of weighting is consistent with the vertical structure of SPOM. Terms involving free surface variables use the weight factor $\frac{\eta}{H}$ while ocean bottom variables use the weight factor $\frac{\Delta z_{bot}}{H}$.

Chapter 4

Results

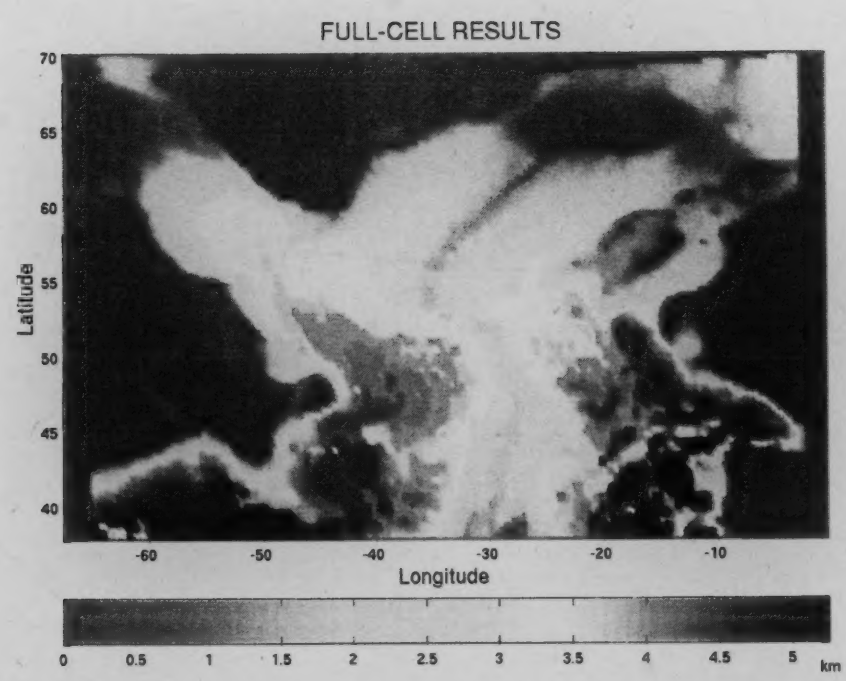

Figure 4.1: Full-cell representation of the subpolar gyre domain used in our experiments.

4.1 Balances of the Vorticity Equations

The two numerical experiments previously outlined are conducted on two fourty year integrations of SPOM performed by Myers (2002). One experiment uses a full-cell topography representation while the second uses partial-cells. The individual terms of the two vorticity equations discussed in Chapter Two are computed and analyzed for both experiments. In 2002, Myers conducted this pair of experiments and focused on differences in large-scale circulation and water formation patterns in the subpolar North Atlantic between the full and partial-cell implementations of SPOM. He discovered that the partial-cell version produced an improvement in transport values, a tighter and sharper gyre structure, a series of sub-polar mode water formation sites linked to gyre topography, and a reasonable representation of Labrador Sea water formation and dispersal. Our objective is to determine if the partial-cell implementation of SPOM will produce similar improvements in the vorticity balance.

Model output has been averaged over one modelled year to increase the length of the averaging period and thereby reduce the size of the temporal terms not included in our calculations. No significant changes occurred when the period of the time average was increased from one to ten years, with the biggest differences being slight decreases in the calculated tendency near the Grand Banks and the Flemish Cap.

4.1.1 Barotropic Vorticity Equation

The overall balance of the barotropic vorticity equation holds to $O(10^{-6})$ s^{-2} as illustrated in Figure 4.2. In the full-cell case, most of the vorticity fluctuations are limited to steep topographic boundaries surrounding the sub-polar gyre. The few fluctuations occuring in the gyre interior seem to be topographically bound as well. Two examples are the fluctuations in the northwest gyre arm and positioned over Reykjanes Ridge. The partial-cell model also exhibits the topographical binding of vorticity fluctuations. However the larger and faster current patterns lead to more small-scale vorticity fluctuation in the gyre interior. The northward flowing countercurrent near the Labrador coast and the Eastern Greenland Current (which is situated more offshore in the partial-cell case) both create areas where this interior vorticity fluctuation is present.

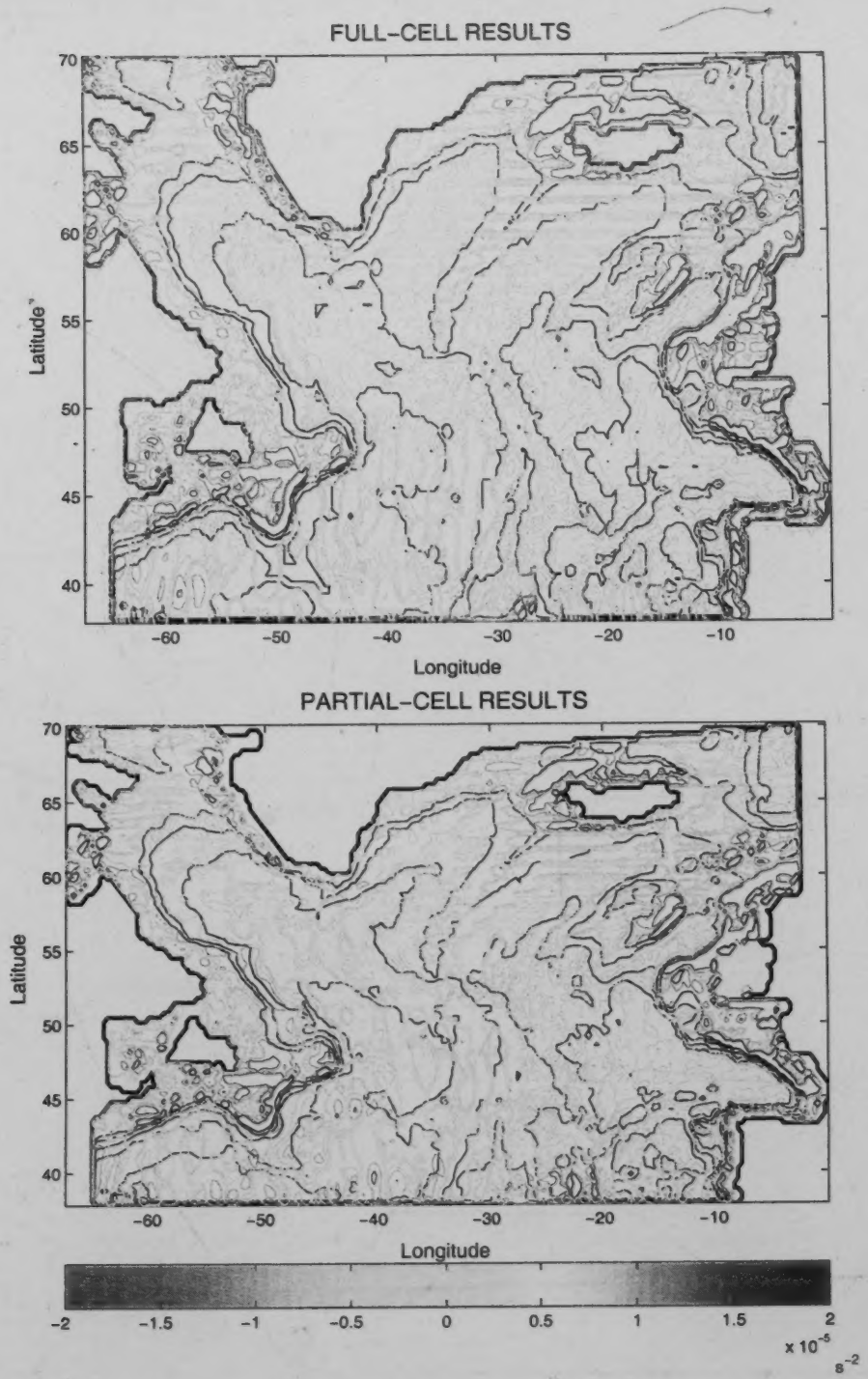

Figure 4.2: Computed sum of the individual terms in the barotropic vorticity equation for the entire subpolar gyre domain.

The largest fluctuations occur in regions with strong, energetic currents. Regions associated with significant circulation variability include the Gulf Stream-Labrador Current interaction zone ($35 - 50^oW, 40 - 48^oN$), the East Greenland Current as it passes Cape Farewell and encounters Eirik Ridge ($38 - 48^oW, 57 - 61^oN$), along the Labrador continental shelf ($51 - 60^oW, 52 - 60^oN$), and Reykjanes Ridge ($25 - 32^oW, 57 - 64^oN$). These features are more clearly seen in the partial-cell model due to its more robust circulation and significant variability(Myers, 2002). This is consistent with Myers and Deacu (2003) who found significant model eddy activity associated with enhanced eddy kinetic energy along the Labrador slope. They also found that eddy kinetic energy was much smaller in the gyre interior in both the full and partial-cell models. Differences between the full and partial-cell experiments can also be seen over the Mid-Atlantic Ridge at $25 - 35^o$ longitude and in the Norwegian Sea.

Figure 4.3 shows the full and partial-cell Coriolis fields for the barotropic vorticity equation. As expected, the field magnitudes are highly dependent on the resolved current structures. With its stronger and more robust resolution of the current patterns, the partial-cell model exhibits much greater magnitudes and structure in its Coriolis field. The resolved meridional currents of the subpolar gyre domain form a significant portion of the Coriolis field especially when one compares the field to the resolved meridional current structure (Figure 4.4). Both models represent all the major current structures in the sub-polar gyre however there are some significant dif-

ferences between the two experiments. The partial-cell results reflect better resolved currents whose magnitudes tend to be 2-3 times larger than their full-cell counterparts. Specific differences are also evident between the two experiments. For instance, in the partial-cell experiment there are two distinct southward flowing branches of the Labrador Current- one near the shore and one flowing the continental shelf break. There is a difference in the proximity of the represented East Greenland Current to the continental shelf along Eirik Ridge between the full and partial-cell experiments. A northwardly flowing countercurrent is present in the partial-cell output just off the Labrador continental shelf. For more detail on the changes the partial-cell scheme makes to the modelled circulation in the subpolar gyre domain see Myers (2002).

The nonlinear advection field describes the horizontal momentum flux or, in other words, the momentum generated by interaction between the two horizontal velocity fields. These terms are significant in boundary currents where flows are intensified and interact with each other and the boundary's topography. The East Greenland Current, Labrador Current and North Atlantic Current contain the dominant magnitudes of the nonlinear advection field as illustrated in Figure 4.5. The field's magnitude is an order smaller then that of the Coriolis and stress fields. Therefore, it appears to be only a minor component in the determined vorticity balance. However, the nonlinear advection contains more structure and significantly larger magnitudes in the partial-cell experiment.

The stress field consists of a group of terms representing wind stress on the free

surface and frictional stress along the ocean bottom. Combined with the nonlinear advection field, it forms the largest force that helps to balance the Coriolis field. Its influence increases inversely with depth thus it is most significant in shallow coastal waters. The partial-cell model has a much stronger frictional component in its stress field arising from the larger ocean-bottom currents (Figure 4.6).

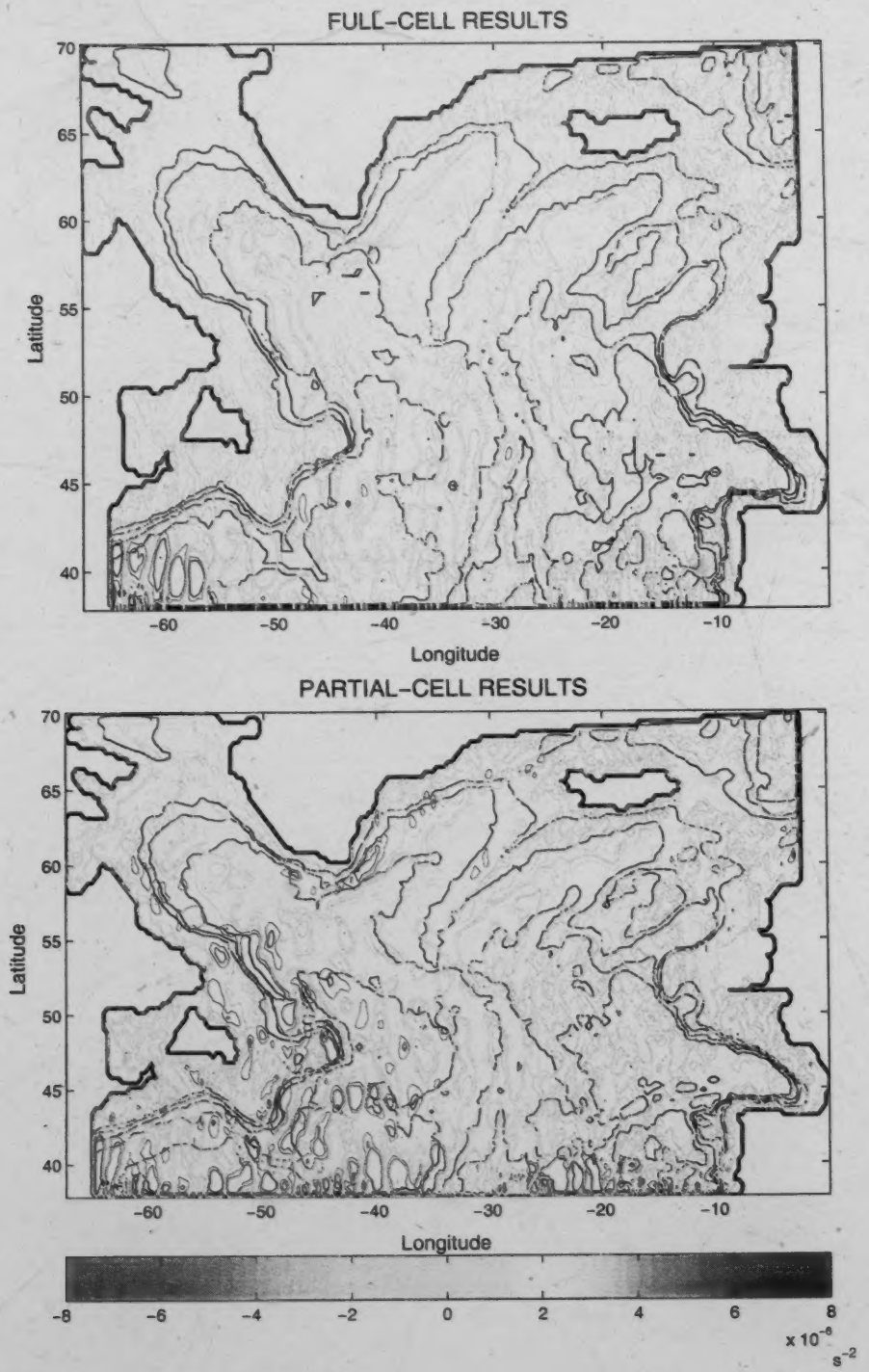

Figure 4.3: Computed magnitudes for the Coriolis term arising in the barotropic vorticity equation.

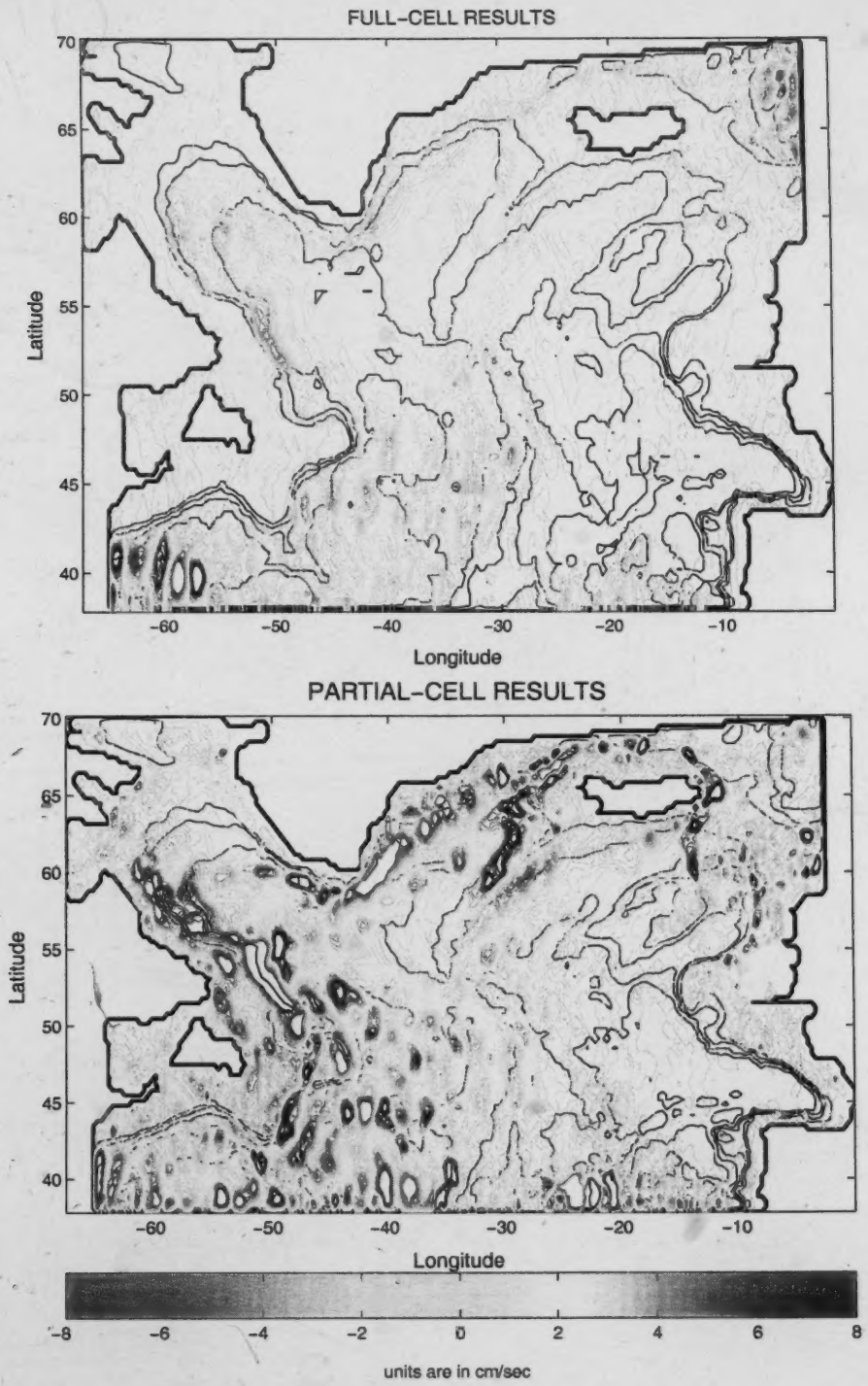

Figure 4.4: Computed magnitudes for the depth-averaged meridional current velocities in the sub-polar gyre domain.

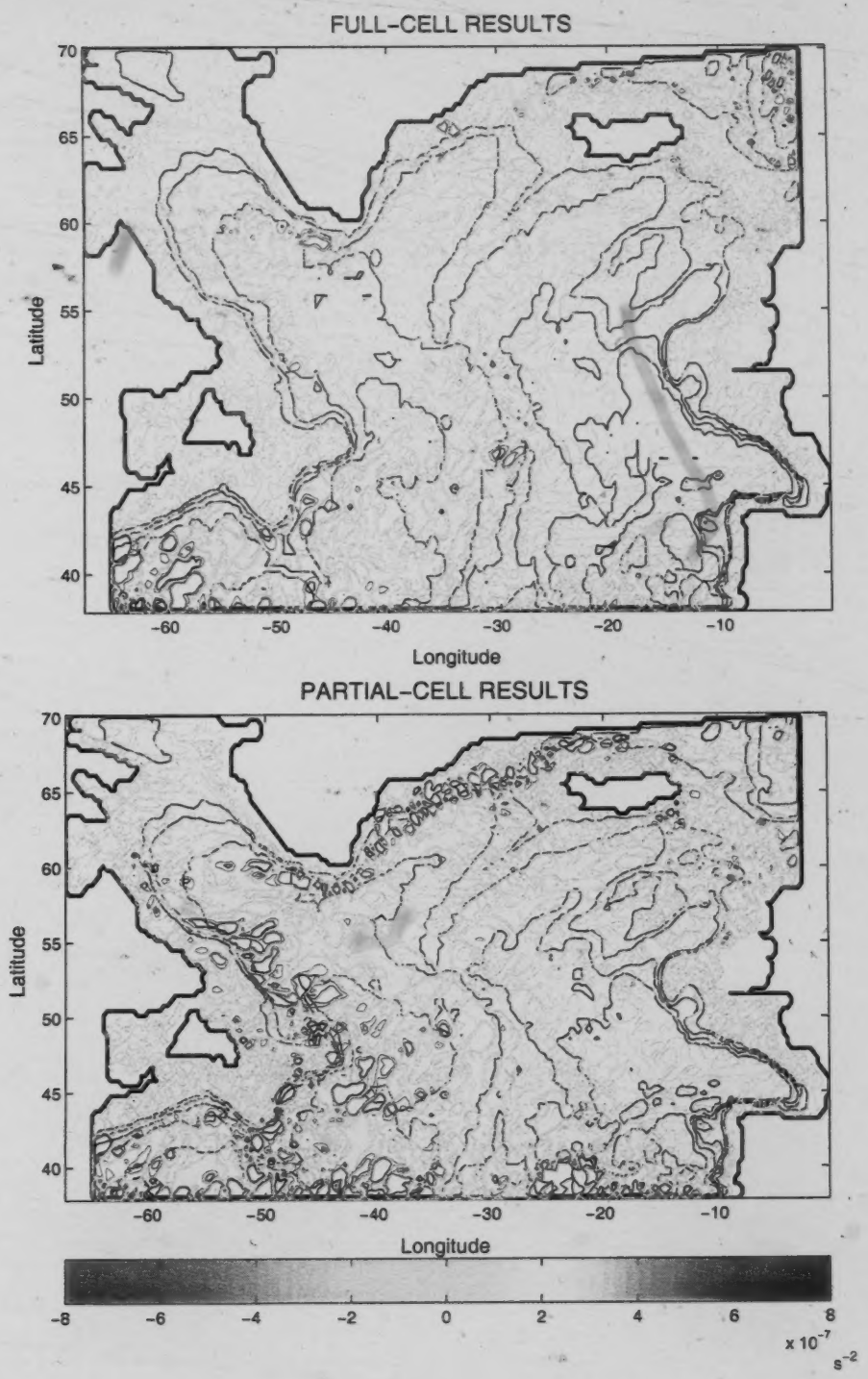

Figure 4.5: Computed magnitudes for the non-linear advection term arising in the barotropic vorticity equation.

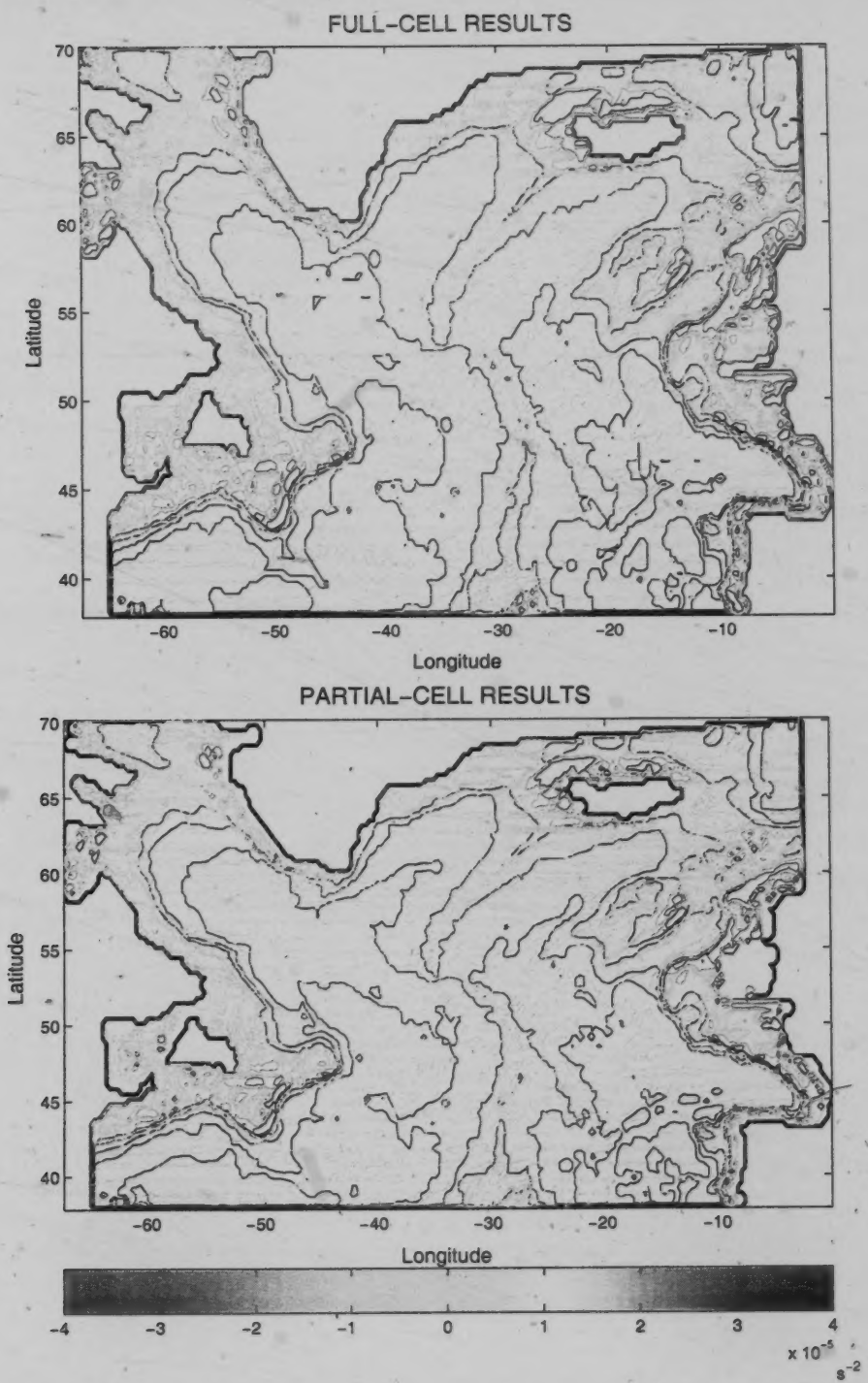

Figure 4.6: Computed magnitudes for the external stress terms (wind and bottom friction) found in the barotropic vorticity equation.

4.1.2 Vorticity Equation for the Depth-Averaged Flow

The overall balance for the vorticity equation of the depth-averaged flow is $O(10^{-5})$ s^{-2}. Again the Coriolis field is a significant factor as most fluctuations occur in regions with strong currents. The presence of the pressure jacobian field increases the influence of the topography in the overall vorticity balance especially in the full-cell experiment. Both experiments see increased vorticity fluctuation near the Labrador and Greenland continental shelves.

Figure 4.8 illustrates the computed pressure jacobian fields for the full and partial-cell models. The bottom pressure jacobian term, $J(H, p_{BOT})$, along with the wind stress, is the most significant factor in the overall balance of the vorticity equation. The jacobian term tends to have its largest values in regions containing steep topographic gradients. Two interesting examples of these regions include Eirik Ridge (southwest of Cape Farewell, Greenland) and along the Labrador continental shelf near Hamilton Bank. At Eirik Ridge, severe topographical gradients along the Greenland continent impose a considerable influence on the jacobian magnitudes. At Hamilton Bank, there is a significant interaction between the sloping topography and the large-scale circulation. Figure 4.8 has been contoured so as to clearly display the large field magnitudes arising from topographic variations. The field also contains smaller scale values, $O(10^{-5})s^{-2}$, arising from density stratification and are more centrally located within the gyre.

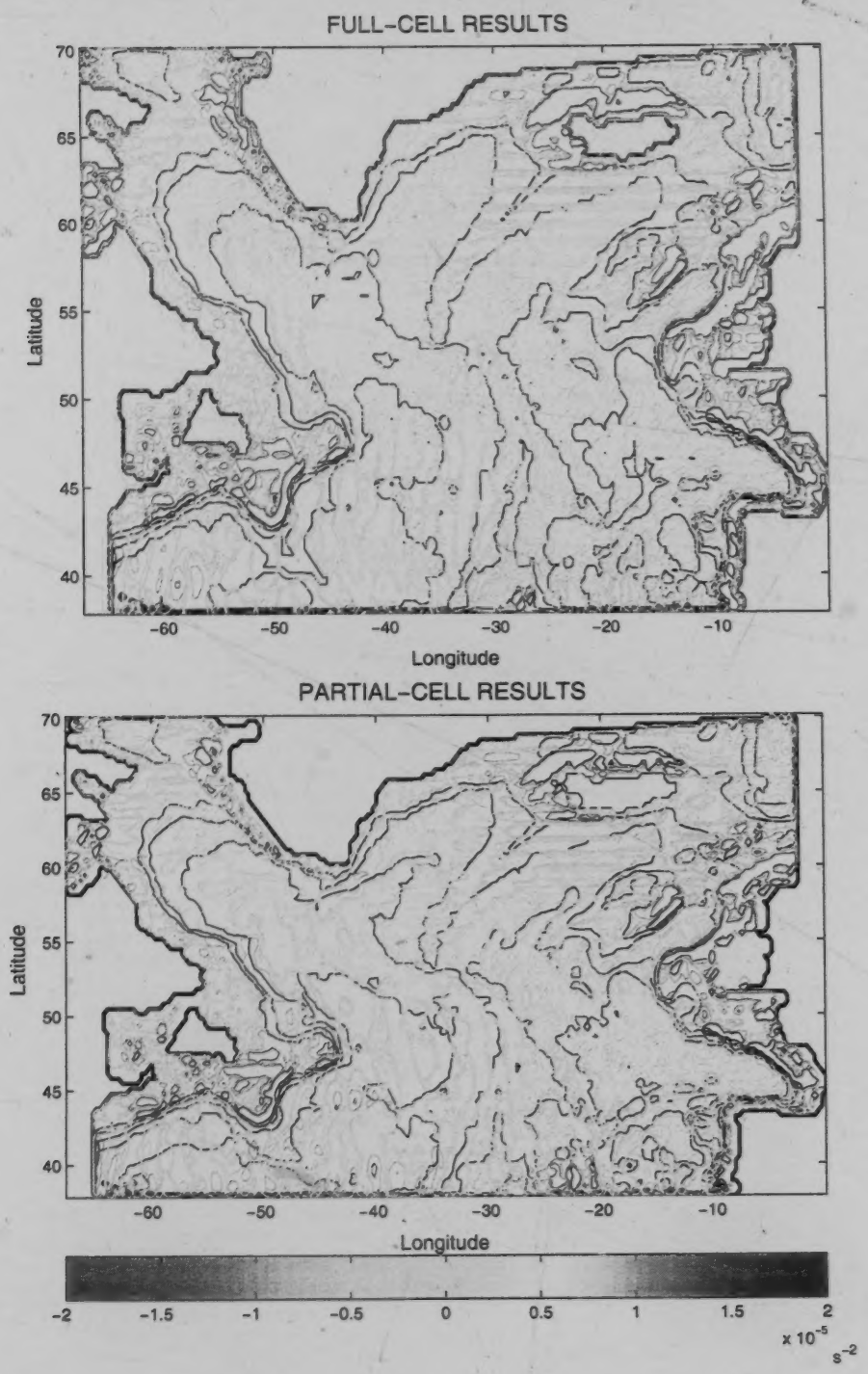

Figure 4.7: Computed sum of the individual terms arising in the vorticity equation for the depth-averaged flow.

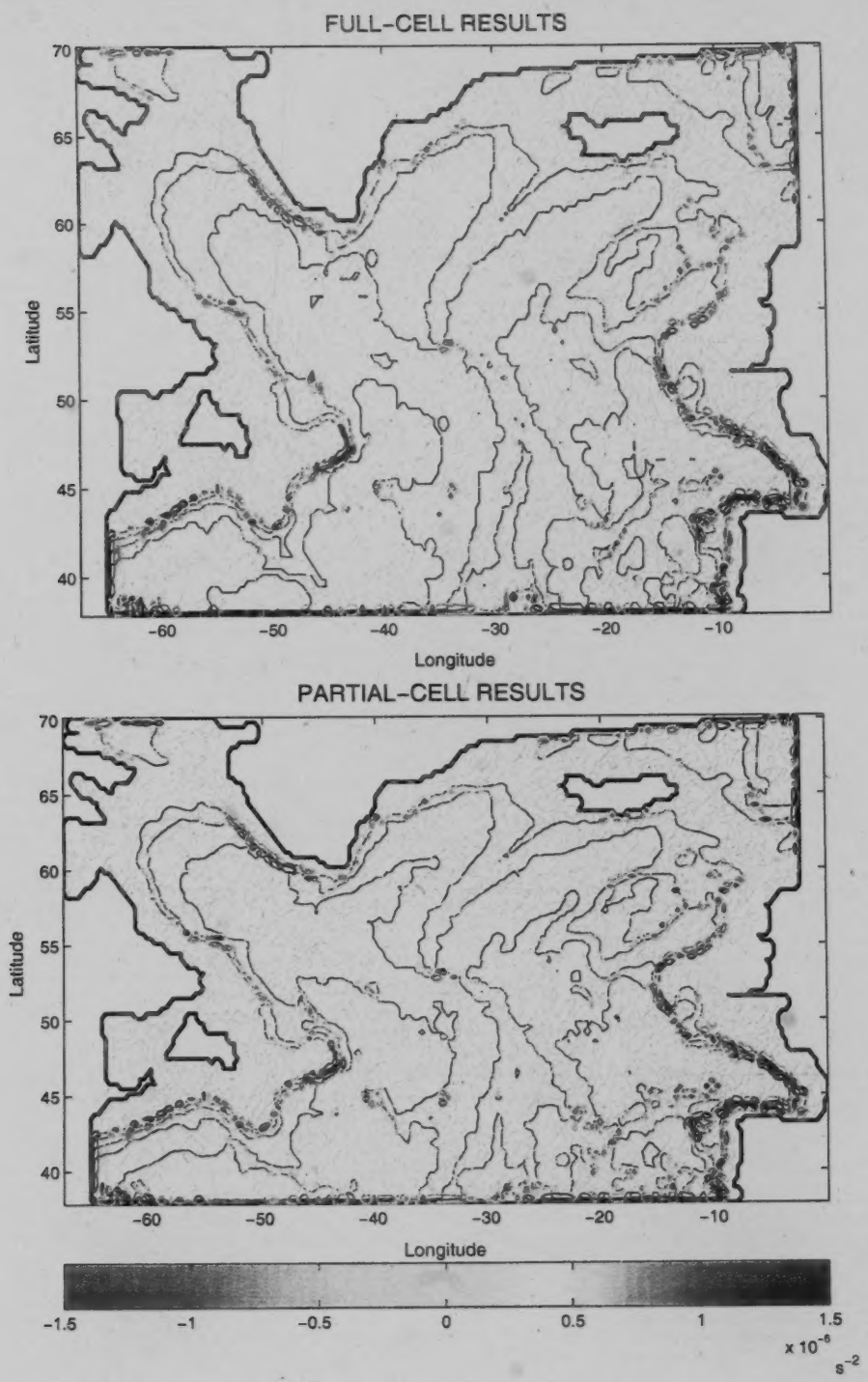

Figure 4.8: Computed magnitudes for the explicit JEBAR term appearing in the vorticity equation for the depth-averaged flow.

4.2 Overall Balance of Vorticity Equations at Specific Geographical Sites

We have observed that the overall imbalance in the vorticity equations tends to accumulate in areas containing large topographic gradients and strong interacting currents where we expect variability. Two specific geographic locations were chosen to illustrate these results.

4.2.1 Eirik Ridge

Eirik Ridge is a southwestern protrusion of the Greenland continental shelf extending 41-45^oW and $58.5 - 59.5^oN$. This region contains severe topographic slopes (along the Greenland continental shelf), two major boundary currents (the East and West Greenland Currents), and is the location where the East Greenland Current separates from the southern tip of Greenland(Cape Farewell).

Barotropic Flow

Eirik Ridge is comprised of a steep southwest slope extending from the coastline to a small knoll at $\approx 58.5^oN$ followed by a sharp decline into the deep interior. The knoll appears to be a key topographical influence on the East Greenland Current as it rounds Cape Farewell. In the full-cell model, the East Greenland Current closely follows the continental shelf with a majority of the current flowing to the outside of the lower knoll before turning northward. The stronger partial-cell East Greenland

Current is not as tightly bound to the continental shelf so the knoll shears part of the flow into the northward West Greenland Current. The other component of the flow separates southwestward forming a jet. Figure 4.9 illustrates the differences in the barotropic flow between the two experiments.

Overall Balance of the Barotropic Vorticity Equation

There seems to be less variability in the immediate area of the lower knoll in the full-cell results (Figure 4.10). This can be attributed to the full-cell East-West Greenland Current structure being more bound to the continental shelf thereby lowering the amount of impact between the flow and the lower knoll. As stated previously, in the partial-cell model the lower knoll divides the incident East Greenland Current into a northward boundary current and westward current that crosses the western arm of the subpolar gyre. Partial-cell vorticity fluctations follow and highlight this current division with a strong southward flowing jet present in the experiment. Both experiments have a large amount of vorticity fluctuation occuring along the West Greenland continental shelf. The most probable explanation for the fluctuation is that steepness of the continental shelf is such that both topographic representations exhibit the staircase effect along the shelf. Some of the vorticity fluctuation could be the result of misrepresentation of gravity wave interaction with the topography (referred to as "gravity noise" by Adcroft et al.(1997)). The series of steps representing the West Greenland continental shelf in the numerical model form a series of vertical

barriers that is struck by some of the northwardly diverted flow from Eirik Ridge. When any flow glances the vertical barrier there is a sudden and dramatic change in the vertical component of the flow. To maintain a consistent energy balance, the numerical ocean model artifical introduces additional vertical flows fluctuations offshore from the shelf.

Figure 4.11 shows the magnitudes of the individual terms of the barotropic vorticity equation along 59.1667^oN extending 34-54^oW. The Coriolis field is dominant in both models as its magnitude is controlled by the strong currents surrounding Eirik Ridge and the high latitude at which the ridge is located. Current velocities are higher in the partial-cell model and thus the corresponding Coriolis field reflects this with higher peaks at 47^oW (West Greenland Current) and 42.5^oW (East Greenland Current). Notice that the peaks in the Coriolis field are sharper in the partial-cell output. The full-cell stress field is relatively constant except over the lower knoll where the ocean depth decreases. A smoother representation of the lower knoll does not lead to any major peaks in partial-cell stress field. The maximum values of the non-linear advection field occur between 45-51^oW in both experiments. The magnitudes of the partial-cell model are largest and its nonlinear advection field has a wider peak structure in the beforementioned longitude range. This is probably a result of interaction between the both the continental shelf and the lower knoll on the incident East Greenland Current. Also, the partial-cell model contains two separate current structures at this location (West Greenland Current and the westward offshooting

current) which most likely interact with each other.

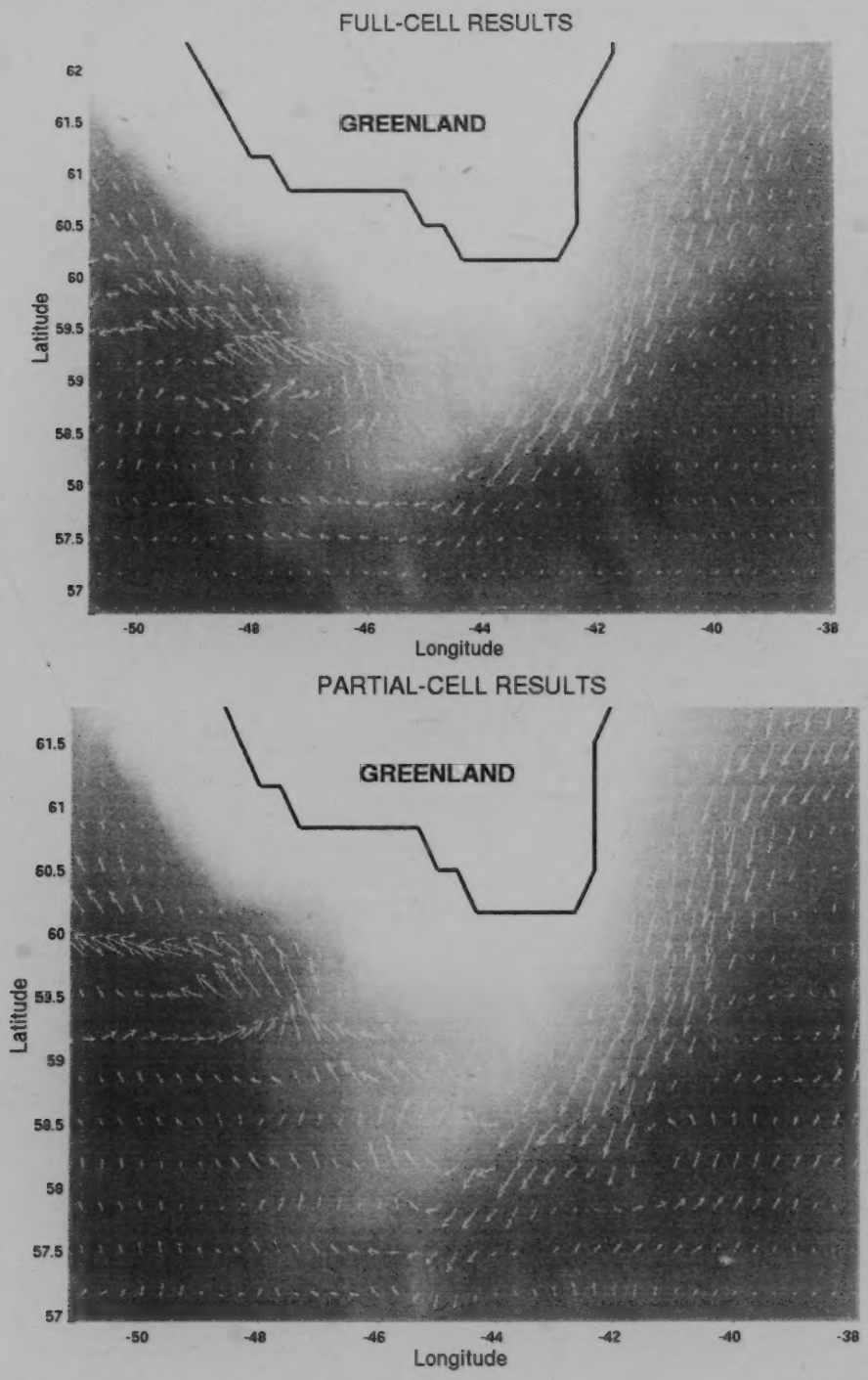

Figure 4.9: Barotropic flow around Eirik Ridge predicted by current data from the Sub-Polar Ocean Model.

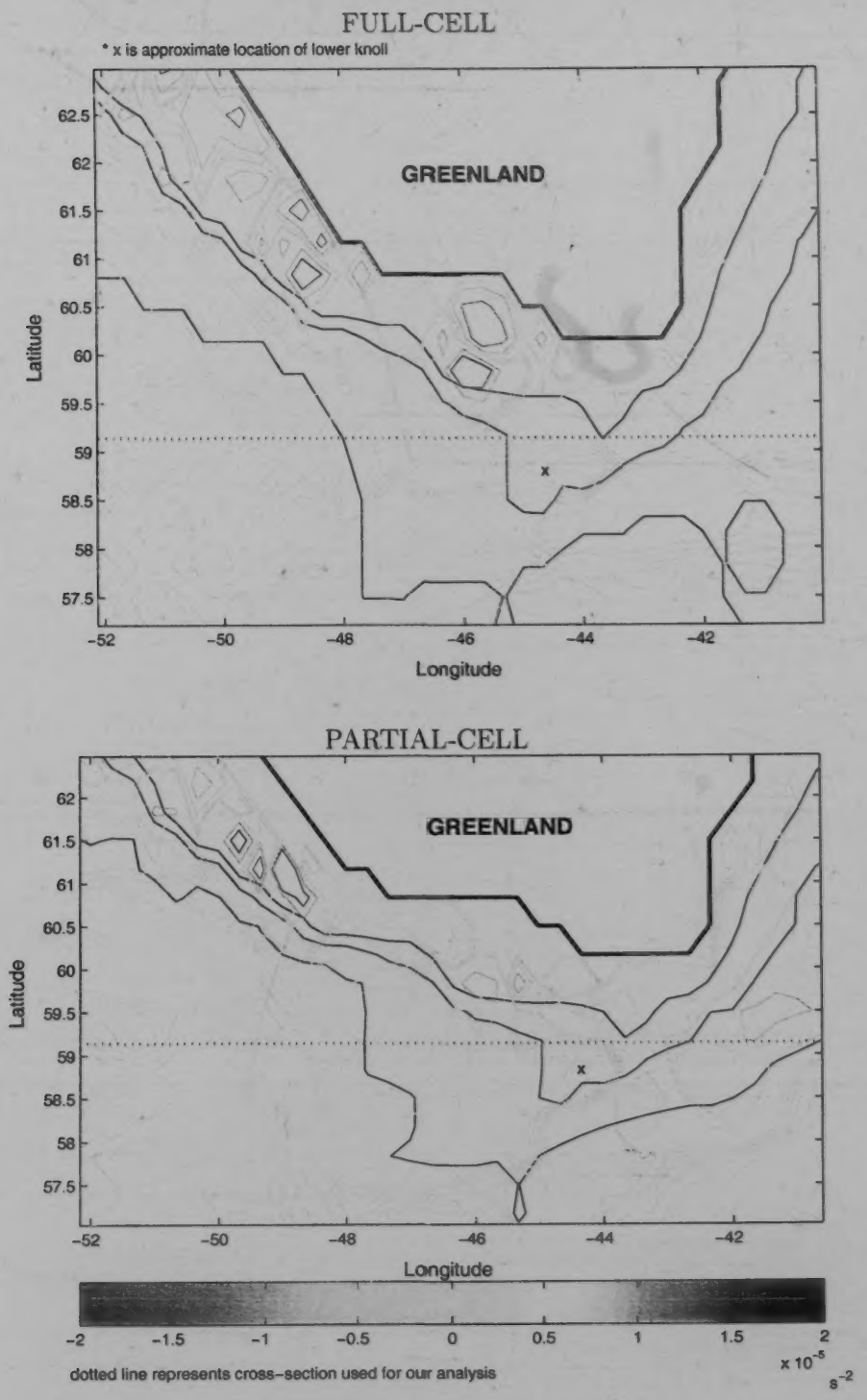

Figure 4.10: Sum of the individual terms arising in the barotropic vorticity equation around Eirik Ridge.

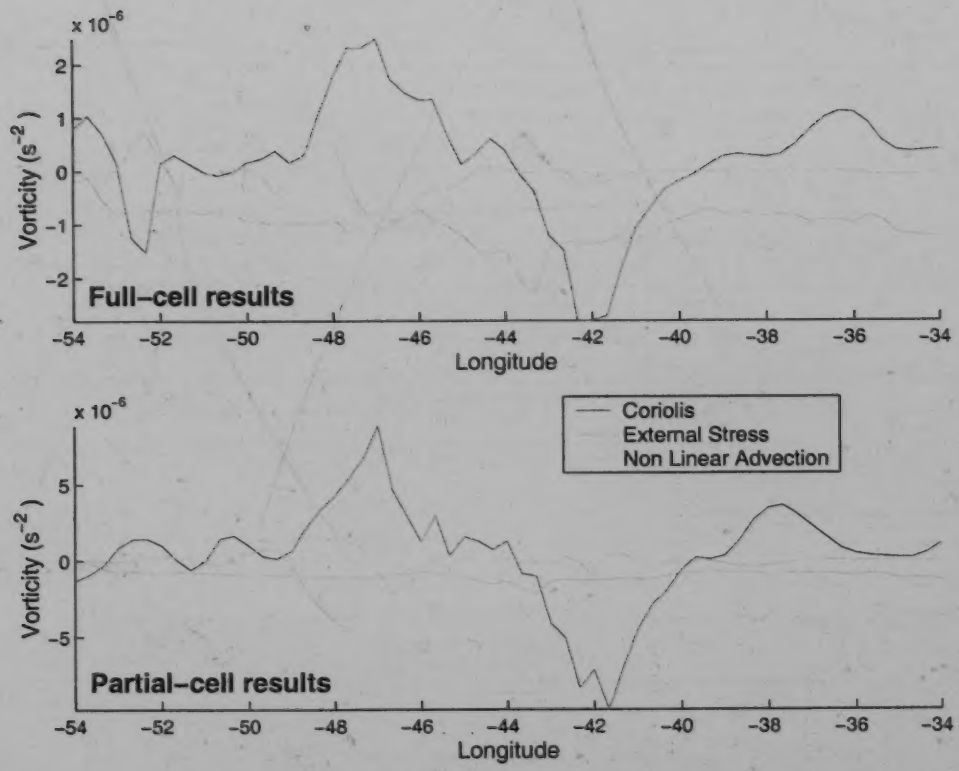

Figure 4.11: Magnitudes of the three dominant terms in the barotropic vorticity equation along a zonal cross-section ($59.1667^{o}N$). The cross-section is denoted by the red dotted line in Figure 4.10.

Overall Balance of the Vorticity Equation for the Depth-Averaged Flow

Figure 4.12 shows the overall balance around Eirik Ridge. The partial-cell output clearly illustrates the beforementioned splitting of the East Greenland Current into the West Greenland Current and a southward flowing jet. Both experiments exhibit a great deal of vorticity fluctuation along the steep continental shelf of western Greenland -an area known to have high variability and a maximum in eddy kinetic energy seen in both satellite and float data(Heywood et al., 1994; Frantantoni, 2001; Cuny et al., 2002). The fluctuation is more tightly bound to the shelf in the partial-cell case however its magnitude remains the same for both experiments. This seems to suggest that extreme increases in depth along the shelf cannot be adequately compensated for by using either topographic representation. In other words, unphysical overshooting and gravity noise is present in both the full and partial-cell models for this particular location, consistent with the idea that partial cells work best in regions containing weak topographic variation.

Figure 4.13 shows the magnitudes of the individual fields along 59.2°N extending from 34° to 54°W. The East and West Greenland Currents are the dominant features in both experiments. There is an interesting development in the area between the lower knoll and the main continental shelf. In the full-cell case, we have a slower moving East Greenland Current striking the northward face of the lower knoll. This results in a northward flow from the knoll along the Greenland shelf as illustrated by the northward peak at 44.5°W in the Coriolis field which has the meridional

current as a controlling feature. The partial-cell East Greenland Current is faster and further away from the continental shelf. Thus, only part of the current glances off the northward face of the lower knoll and retains its southwestwardly direction. No significant peak in the Coriolis field occurs at 44.5°W in the partial-cell experiment. This current splitting process is also evident in the barotropic flow around the lower knoll as shown in Figure 4.9.

We now investigate the two components of the pressure field: topographic and ocean-bottom pressure gradients. As one would expect the two components are intimately connected as shown in Figure 4.14. The severe drop along the Greenland continental shelf results in huge pressure gradients in both models. Notice how the full-cell pressure gradients highlight topographic fluctuations particularly in the case of the smaller topographical features to the southeast of Eirik Ridge and the step-like representation of the middle depth levels to the south of the West Greenland Current.

4.2.2 Hamilton Bank

Hamilton Bank is an elongated knoll-like structure that extends from $53.5-55.5^{o}N$ and $53\text{-}56^{o}W$ along the Labrador shelf. Major currents that flow in the immediate proximity of Hamilton Bank include the Labrador Current, the North Atlantic Deep Undercurrent, and finally a northward countercurrent on the offshore flank of the boundary current.

Barotropic Flow

Figure 4.15 shows the barotropic flow around Hamilton Bank. In both experiments the southward flowing Labrador Current and North Atlantic Deep Undercurrent are visible. However the northward countercurrent is clearly distinguishable only in the partial-cell experiment. Three standing eddies are observed in the full-cell results located at $(60.5^oW, 57^oN)$, $(57.5^oW, 55.25^oN)$ and $(55^oW, 54^oN)$. Only the most southern eddy is observed in the partial-cell model. These eddies are probably induced by the topographical representation of several small, but deep, basins that lie along the continental shelf. Both z-level representations of topography (full and partial-cell) lead to these features being modelled as a series of holes. This "hole phemonemon" is lessened with partial cells employed as the step topography(Adcroft et al., 1997) is given a more smooth structure.

Significant interaction is seen between the Labrador Current and the countercurrent at $(51^oW, 56^oN)$ in the partial-cell experiment. This is consistent with similar results produced by Deacu and Myers (2003).

The interaction between these currents and the associated instability processes is worth further investigation. The full-cell Labrador Current offshoots Hamilton Bank to a more eastward location potentially impacting the possible penetration of the northward countercurrent into the region. This issue may also deserve further study.

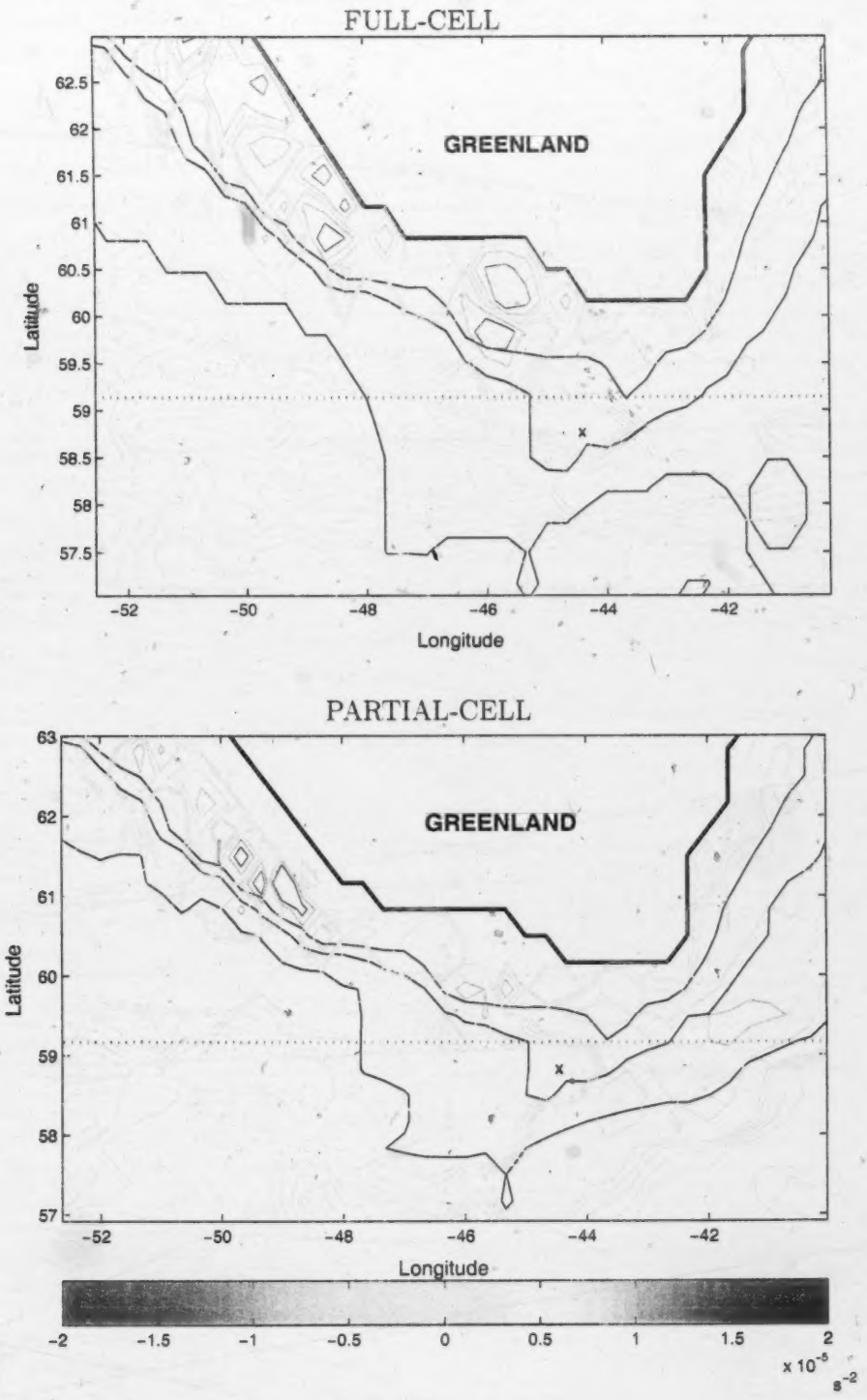

Figure 4.12: Computed sum of the individual terms arising in the vorticity equation for the depth-averaged flow around Eirik Ridge.

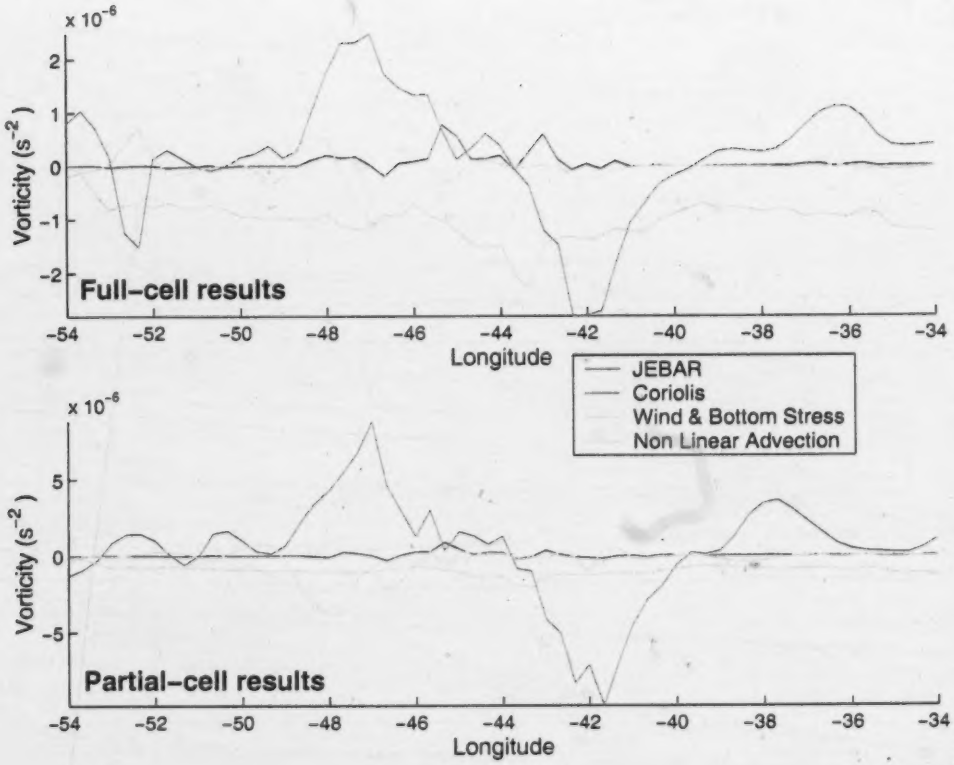

Figure 4.13: Magnitudes of the four dominant terms in the vorticity equation for the depth-averaged flow along a zonal cross-section ($59.1667^{o}N$). The cross-section is denoted by the red dotted line in Figure 4.12.

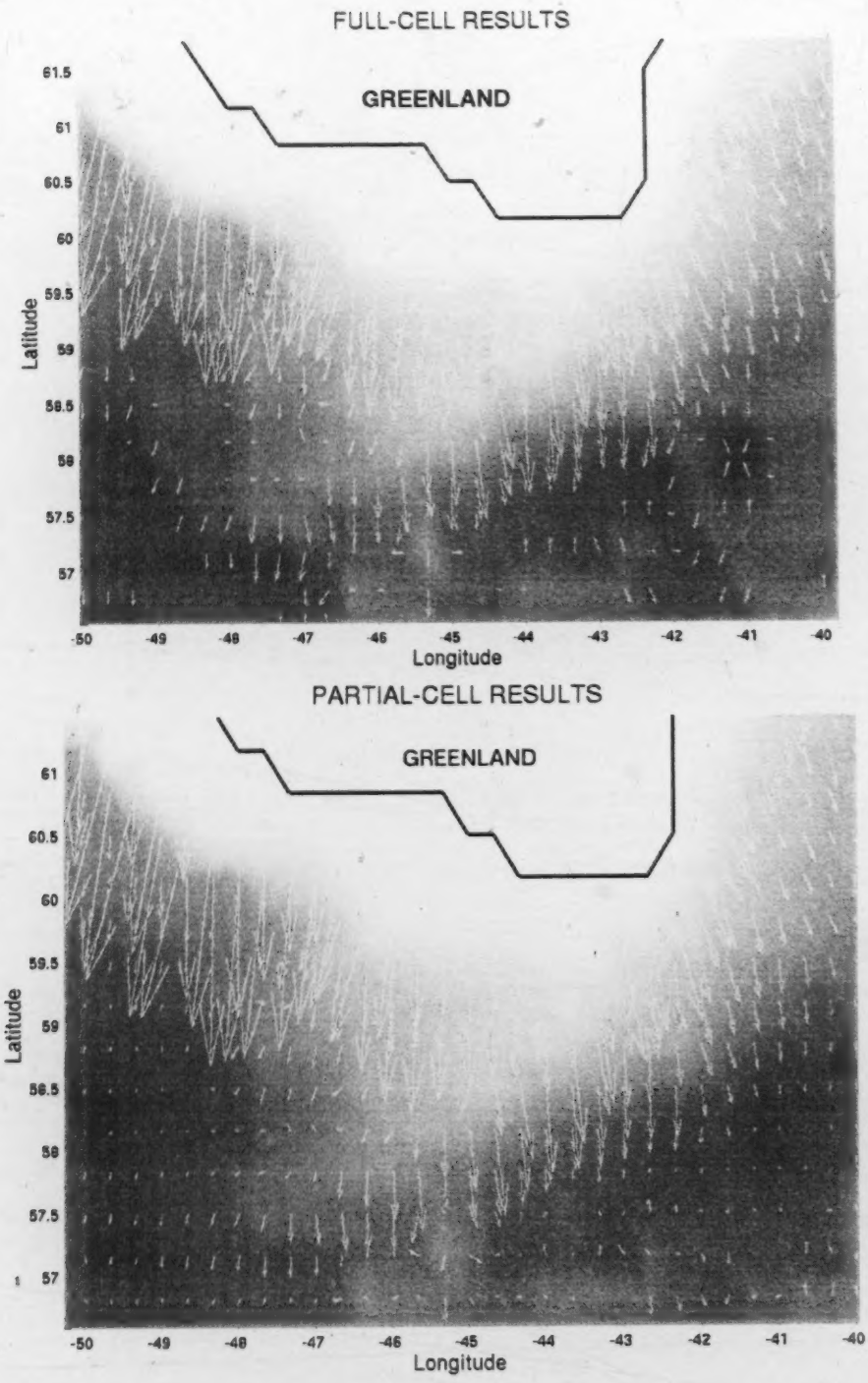

Figure 4.14: Computed ocean-bottom pressure gradient using predicted tracer and topography data from the Sub-Polar Ocean Model around Eirik Ridge.

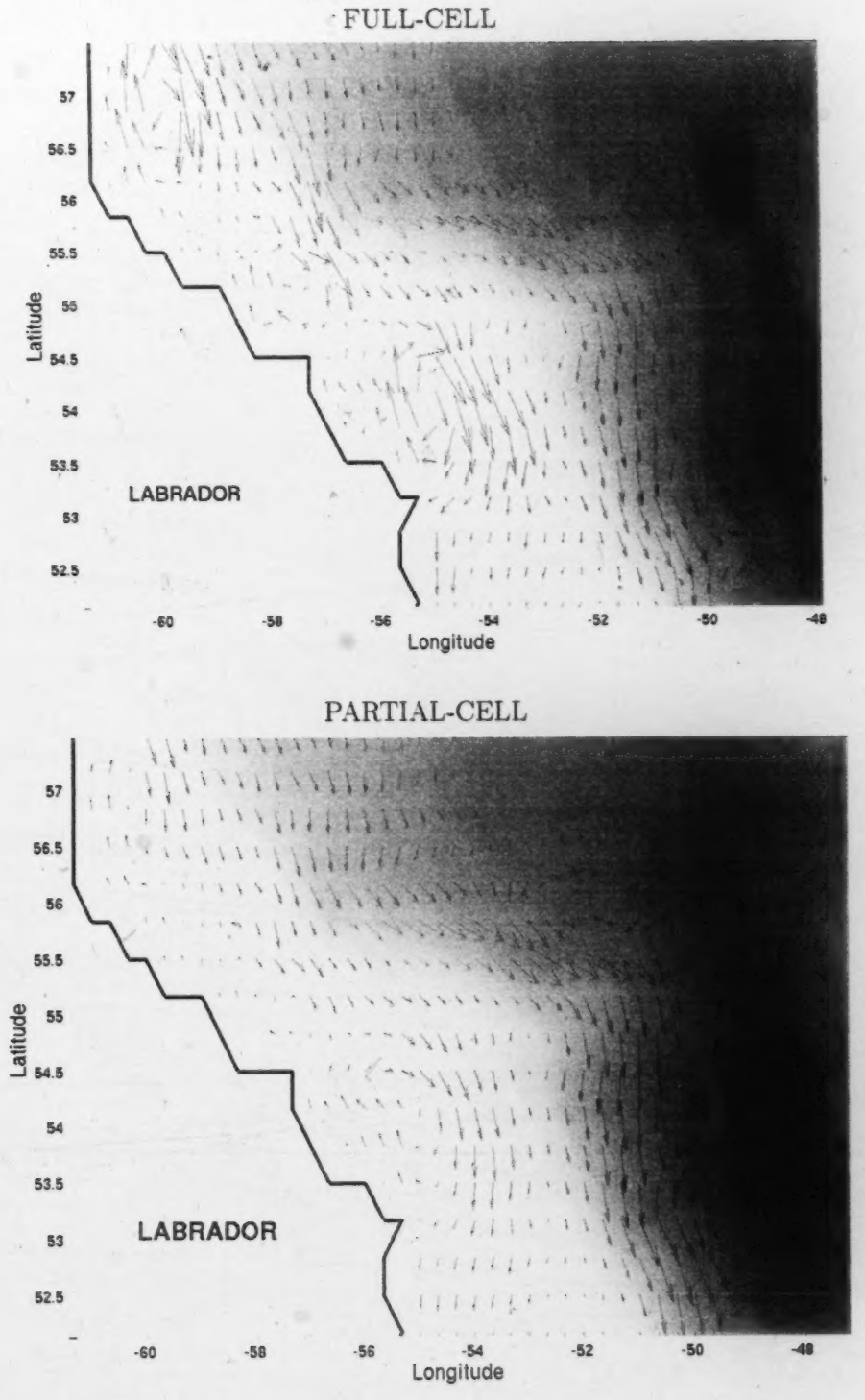

Figure 4.15: Barotropic flow about the Hamilton Bank region predicted by current data from the Sub-Polar Ocean Model.

Overall Balance of the Barotropic Vorticity Equation

Figure 4.16 is a contour plot of the overall balance in the barotropic vorticity equation for the full and partial-cell models. A much stronger Labrador Current and presence of the northward countercurrent highlight the major differences. One can also see the differences on the shelf potentially associated with different eddy circulations. A strong zone of baroclinic instability forms in the partial-cell experiment between the offshore flank of the Labrador Current and inshore flank of the countercurrent consistent with results produced by Myers (2002), Deacu and Myers (2003).

Figure 4.17 shows the magnitude of the individual fields in the barotropic vorticity equation along $55.833^{o}N$. The biggest distinction between the two experiments arises in the dominating Coriolis field. Both experiments exhibit a large southward peaking representing the influence of the Labrador Current and North Atlantic Deep Undercurrent. However, in the partial-cell output, the southward peak is situated closer to the continental shelf and a second southward peak is located at $51^{o}W$ leading to a possible distinction between the two mentioned currents. There is no possible distinction between the two southward flowing currents in the full-cell model. A strong northward countercurrent is present in the partial-cell results.

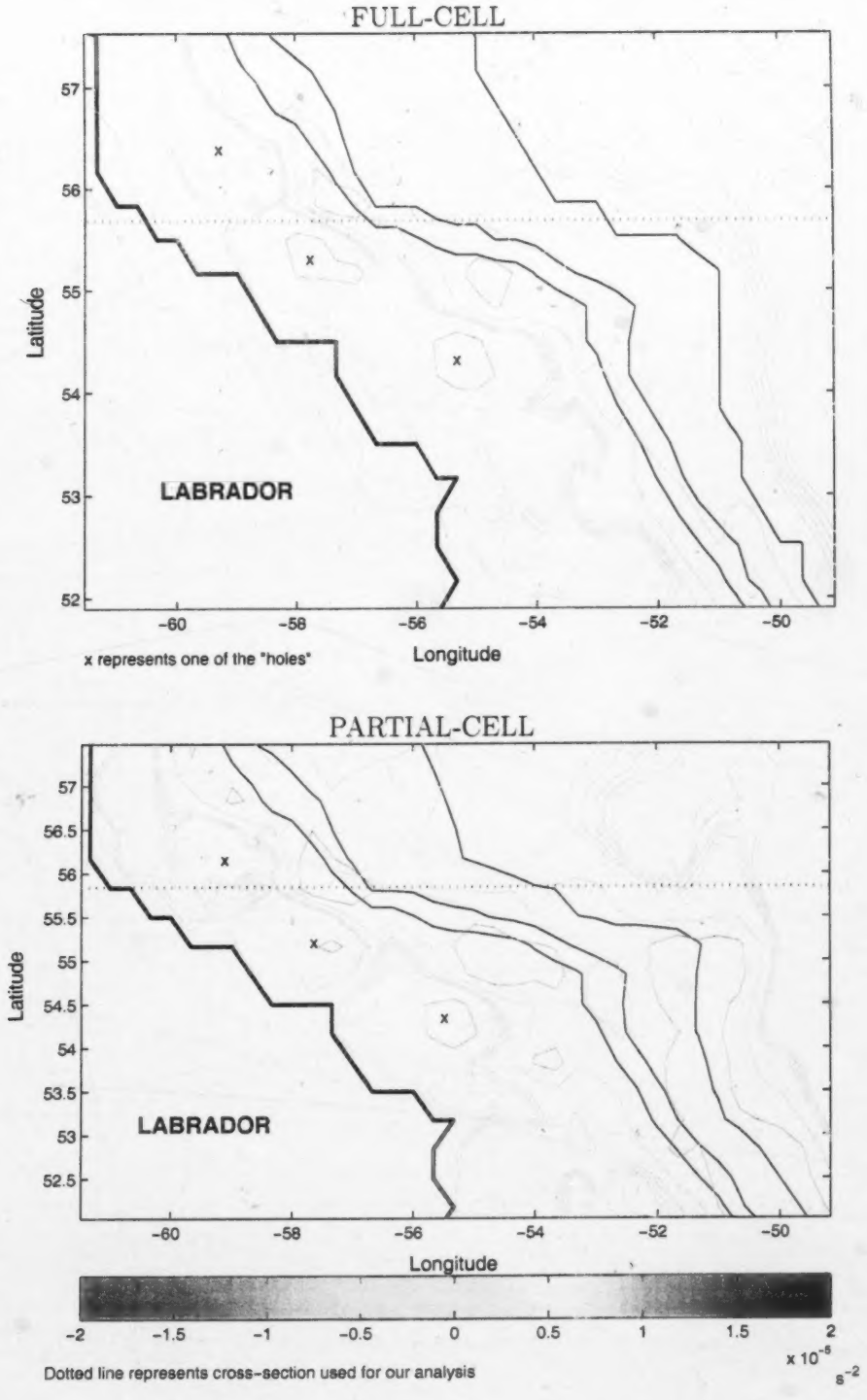

Figure 4.16: Computed sum of the individual terms arising in the barotropic vorticity equation around Hamilton Bank.

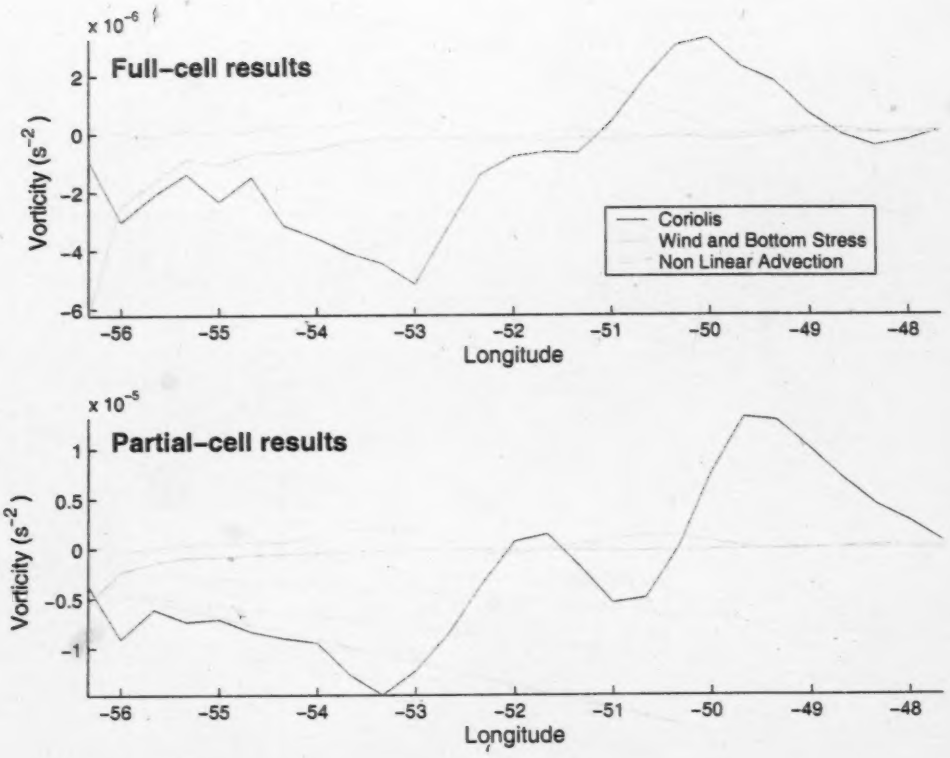

Figure 4.17: Magnitudes of the three dominant terms in the barotropic vorticity equation along a zonal cross-section ($55.833°N$). The cross-section is denoted by the red dotted line in Figure 4.16.

Overall Balance of the Vorticity Equation for the Depth-Averaged Flow

Contour plots of the overall balance of the vorticity equation for the depth-averaged flow are given in Figure 4.18. With its more shoreward location, the partial-cell Labrador Current has more interaction with the topographical features around Hamilton Bank. The most significant topographic influence on the weaker southward full-cell flow is the interaction between the coastal flow and the modelled holes located along the shelf. A similar interaction is present in the partial-cell experiment although it is not the most prevelent feature of the region. With both z-level representations introduce artifical vorticity fluctuations, it would be interesting to compare our results to those achieved with another representation such as sigma-coordinates.

Figure 4.19 shows the magnitude of the individual fields along $55.833^{o}N$. The Coriolis field is again the dominant field with the partial-cell experiment having better resolution of the three main currents (Labrador Current, North Atlantic Deep Undercurrent and countercurrent) in the region. The partial-cell Labrador Current is smoother as it flows onto and around Hamilton Bank. The full-cell representation creates a sharper depth increase at $53.5^{o}W$ resulting in a sudden pressure fluctuation that effects the magnitude of all the individual fields.

The gradient of the ocean-bottom pressure is almost the same for both experiments as seen in Figure 4.20. The slope of the continental shelf produces the dominant values as it is large enough to negate the improvements created by the partial-cell topographic representation. Small-scale pressure convergences are present in both ex-

periments at $(59°W, 56°N)$, $(56.5°W, 54.5°N)$ and $(54°W, 53°N)$. These convergences seem to coincide with the modelled holes along the continental shelf. The validity and physical significance of these convergences could be the subject of future investigations.

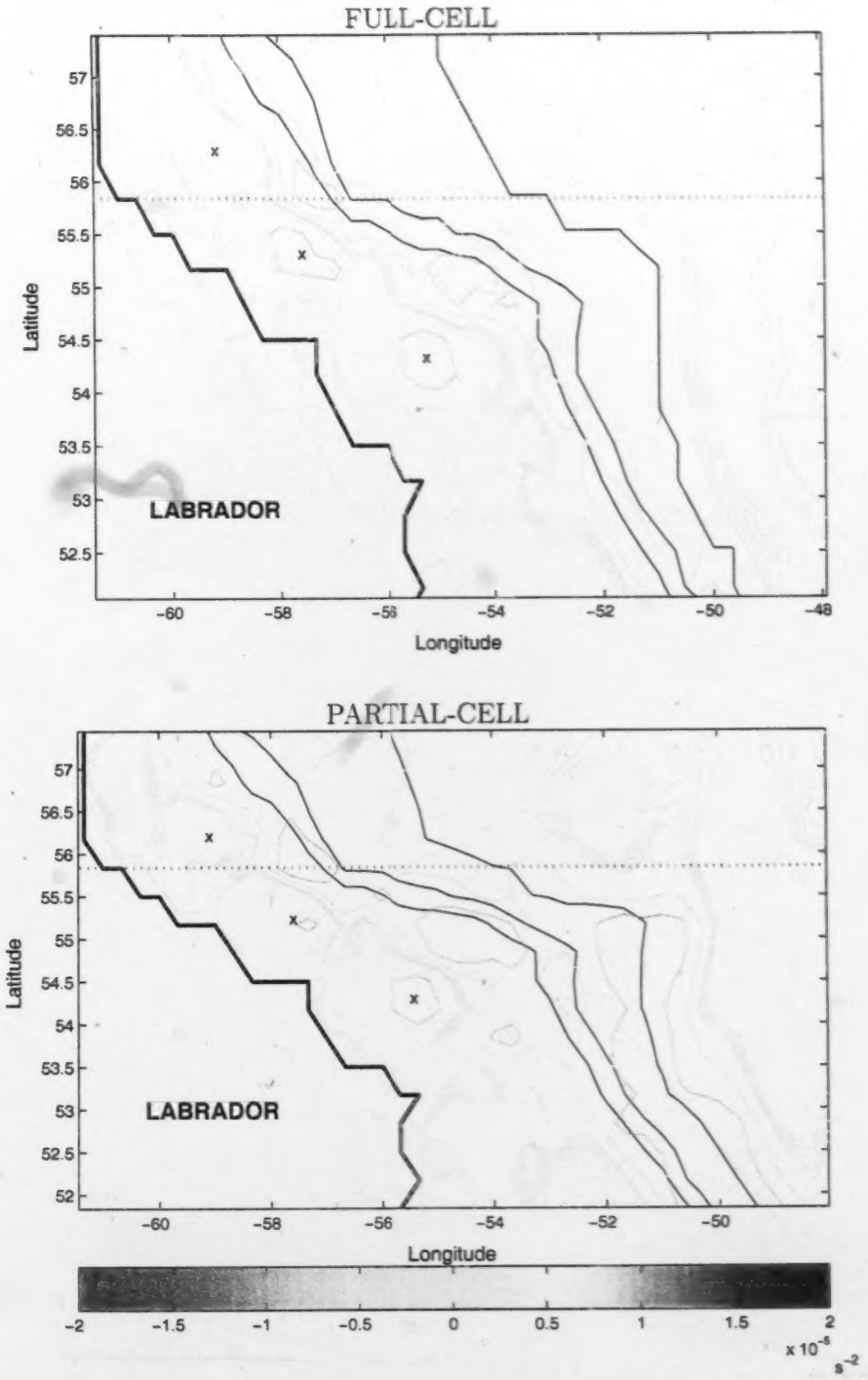

Figure 4.18: Computed sum of the individual terms arising in the vorticity equation for the depth-averaged flow around Hamilton Bank.

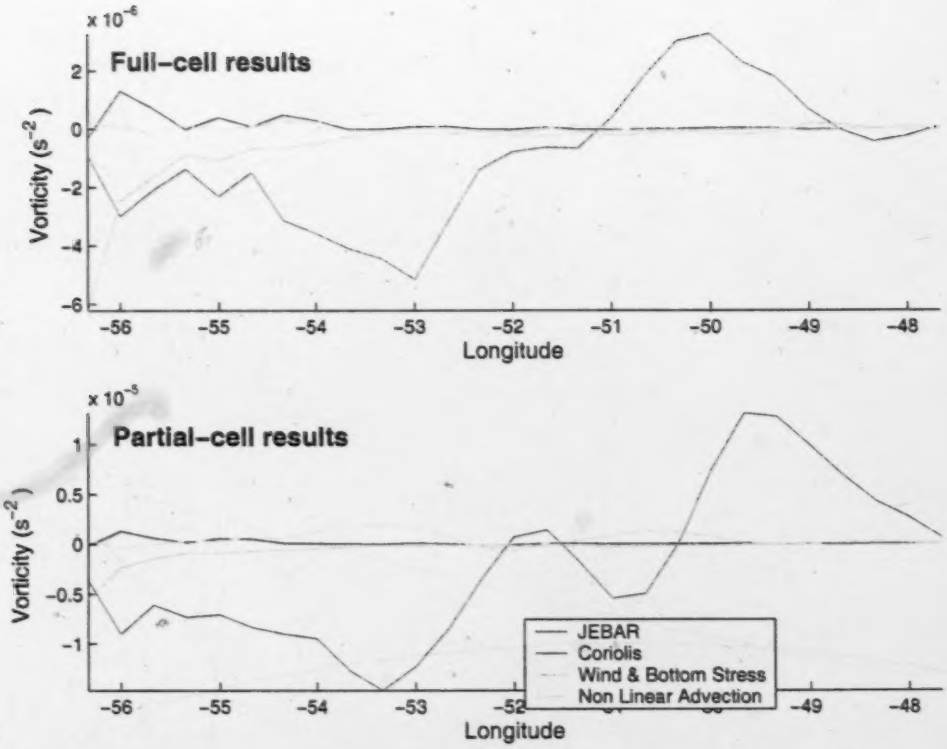

Figure 4.19: Magnitudes of the four dominant terms in the vorticity equation for the depth-averaged flow along a zonal cross-section ($55.833^{o}N$). The cross-section is denoted by the red dotted line in Figure 4.18.

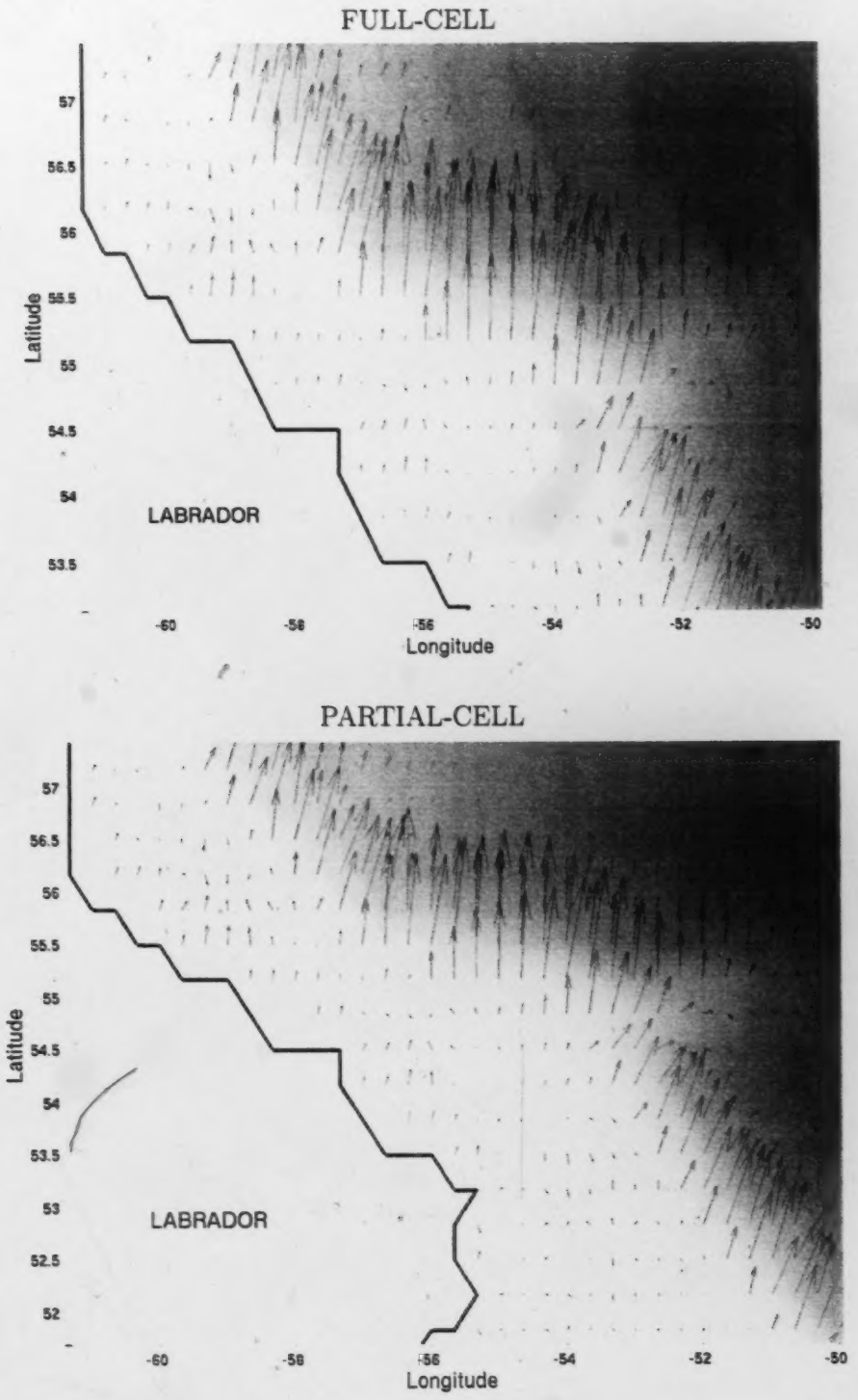

Figure 4.20: Gradient of ocean-bottom pressure around Hamilton Bank.

Chapter 5

Summary

Partial-cell topographic representation is a simple yet effective method that has been shown to improve large-scale current depiction in z-level ocean general circulation models (Pacanowski and Gnanadesikan, 1998; Käse and Stammer, 2001; Myers, 2002). It involves adjusting the height of the bottommost grid cells so as to more accurately reflect the real ocean depths. This adjustment results in a smoothening of small- to medium-scale topographic slopes and determining of more accurate estimate of the individual water column volumes. Partial-cell models utilize the existing finite-difference code for traditional full-cell models so the additional computational costs are acceptably small (Hirsch, 1990).

The Joint Effect of Baroclinicity and Relief or JEBAR (Sarkisyan and Ivanov, 1979) has numerous physical intepretations and numerical descriptions. When one writes the vorticity equation for the depth-averaged flow JEBAR assumes the form of a jacobian operator acting on the ocean-bottom pressure and topography, $J(p_{BOT}, H)$.

The Jacobian describes JEBAR as vorticity correction arising from a topographically induced torque on the barotropic flow (Holland and Hirschman, 1972). When one writes the barotropic vorticity equation for the same domain there is no explicit JEBAR term. However, a collection of product terms involving ocean-bottom velocities and topography gradients replace the Jacobian term. JEBAR now can be thought of as a series of artificial momentum sinks and sources (depending on geographical circumstances) that help balance the vorticity equation (Haidvogel and Beckmann, 1999). Notice that both JEBAR descriptions rely on ocean-bottom topography gradients. It is assumed that an improved topography representation will result in an improved estimation of the topographic gradients yielding a better approximation of JEBAR. This is the premise underlying our current investigation.

Using a regional ocean model (Myers, 2002), we conducted an investigation to determine the effects of switching from full to partial-cell topographic representation on the two beforementioned vorticity equations. The Coriolis field is dominant in both experiments with the partial-cell Coriolis field possessing significantly larger magnitudes than its full-cell counterparts. A northwardly flowing countercurrent to the west of the Labrador Current and a southwestwardly flowing jet eminating from Eirik Ridge are present in the partial-cell model. The dominance of the Coriolis field is not significantly reduced by the remaining equation term fields in both experiments. Possible explanations for this include the exclusion of all temporal terms, and the unphysically low magnitudes of the nonlinear advection and diffusion terms.

The largest vorticity fluctuations were observed over areas containing steep topographic gradients such as the Greenland continental shelf. It is believed that these fluctuations result from artifical overflow and gravity noise created by falling water interacting with the z-level topographic representation. The use of partial cells lessen the impact of these two problems. However, the partial-cell representation of regions with complex topography (such as around Hamilton Bank) tends to have little improvement over full-cell representation. Applying a more complicated topography representation, such as using piecewise-linear cells suggested by Adcroft et al.(1997), could be a solution. Another possible solution could be using a terrain-following coordinate model. However, the characteristically smooth topography representation of such models may lead to a masking of subtle topographic features such as the series of depressions lining the Labrador continental shelf.

Both modelled nonlinear equation term fields (advection and diffusion) were unrealistically small, particularly in areas where their magnitudes are expected to be relatively large such as in the Eirik Ridge offshoot jet. We suspect that our assumption that both terms are analytic (so that the differentiation and integration operations can be readily switched in order) may be incorrect. The presence of non-analytic diffusion and advection terms would change our derivations for the two vorticity equations dramatically. The nonlinear advection and diffusion fields could be viewed as instanteous momentum sources and sinks. Therefore the use of annually-averaged velocity data may be degrading our ability to accurately describe these processes.

One could possibly eliminate this restriction by employing a more detailed weighting scheme where more emphasis is placed on current velocities in the upper depth layers.

Two specific geographical areas were examined in greater detail: Eirik Ridge situated at the southwest point of the Greenland continent and Hamilton Bank attached to the Labrador continental shelf. Both sites are good examples of how local topography effects the vorticity balance and structure.

Our investigation spawned a number of ideas that could fuel future work. One idea involves how local topographic features effect large-scale currents. For example, how important is the Eirik Ridge structure in the separation of the East Greenland Current and the resulting structure of the West Greenland? Certain numerical aspects of our investigation could be re-approached. For instance, one could compute the overall balance of each vorticity equation using in-situ data with the inclusion of the temporal term. The annual average of the in-situ balance data could then be determined and compared with our current findings.

There is a definite improvement in the representation of basin-wide flow patterns when one switches from full to partial-cell topographic representation. There is good reason to believe that switching from a partial-cell to a more complex finite-volume model(Hirsch, 1990) (such as a piecewise-linear model(Adcroft et al., 1997)) may bring additional improvements. Switching completely to such a model would incur significant computational costs. However, we have observed that (for the case of vorticity) most fluctuations occur over areas of steep or complex topographic features.

So one could apply the more complex topographic representation to only these selected areas thereby reducing the associated costs.

Bibliography

Acheson, D. (1990). *Introductory Dynamical Oceanography.* Oxford Applied Mathematics and Computing Science Series. Oxford University Press Inc, New York, NY, U.S.A.

Adcroft, A., Hill, C., and Marshall, J. (1997). Representation of topography by shaved cells in a height coordinate ocean model. *Mon. Wea. Review*, 125:2293–2315.

Bell, M. (1997). Vortex stretching and bottom torques in the bryan-cox ocean circulational model. Ocean Applications Technical Note 17, Hadley Centre for Climate Prediction and Research.

Cuny, J., Rhines, P., Niiler, P., and Bacon, S. (2002). Labrador sea boundary currents and the fate of irminger sea water. *J. Phys. Oceanogr.*, 32:627–647.

Frantantoni, D. (2001). North atlantic surface circulation during the 1990's observed with satellite-tracked drifters. *J. Phys. Oceanogr.*, 32:627–647.

Greatbatch, R., Fanning, A., Goulding, A., and Levitus, S. (1991). A diagnosis

of interpentadal circulation changes in the north atlantic. *J. Geophys. Res.*, 96(C12):22009–22023.

Haidvogel, D. B. and Beckmann, A. (1999). *Numerical Ocean Circulation Modeling.* Imperial College Press, London,UK.

Haney, R. L. (1991). On the pressure gradient force over steep topography in sigma coordinate ocean models. *J. Phys. Oceanogr.*, 21:610–619.

Heywood, K., McDonagh, E., and White, M. (1994). Eddy kinetic energy of the north atlantic subpolar gyre from satellite altimetry. *J. Geophys. Res.*, 99:22525–22539.

Hirsch, C. (1990). *Numerical Computation of Internal and External Flows.* Numerical Methods in Engineering. Wiley and Sons Inc., New York, NY, U.S.A.

Holland, W. (1973). Baroclinic and topographic influences on the transport in western boundary currents. *Geophysical Fluid Dynamics*, 4:187–210.

Holland, W. and Hirschman, A. (1972). A numerical calculation of the circulation in the north atlantic ocean. *J. Phys. Oceanogr.*, 2:336–354.

Hughes, C. W. and de Cuevas, B. A. (2001). Why western boundary currents in realistic oceans are inviscid: A link between form stress and bottom pressure torques. *J. Phys. Oceanogr.*, 31:2871–2885.

Huthnance, J. (1984). Slope currents and "jebar". *J. Phys. Oceanogr.*, 14:795–810.

Jeffrey, A. (1995). *Handbook of Mathematical Formulas and Integrals.* Academic Press, San Diego, CA, U.S.A.

Käse, R. and Stammer, D. (2001). On the mid-depth circulation in the labrador and irminger seas. *Geophys. Res. Letters*, 28(18):3433–3436.

Marshall, J., Adcroft, A., Hill, C., Perelman, L., and Heisey, C. (1997). A finite-volume, incompressible navier stokes model for studies of the ocean on parallel computers. *J. Geophys. Res.*, 102:5753–5766.

Mellor, G. and Oey, L. (1993). On the pressure gradient conundrum of sigma coordinate ocean models. Program in Atmospheric and Oceanic Sciences, Princeton University.

Myers, P. G. (2002). SPOM: A regional model of the sub-polar north atlantic. *Atmosphere-Ocean*, pages 445–463.

Myers, P. G. and Weaver, A. J. (1995). A diagnostic barotropic finite-element ocean circulation model. *Journal of Atmospheric and Oceanic Technology*, 12:511–526.

NOAA (1988). Digital relief of the surface of the earth. Technical Report Data Announcement 88-MGG-02, National Geophysical Data Center.

Pacanowski, R. and Gnanadesikan, A. (1998). Transient response in a z-level ocean model that resolves topography with partial cells. *Mon. Wea. Review*, 126:3248–3270.

Pacanowski, R. and Griffies, S. M. (2000). MOM 3.0 manual. available on the internet at www.gfdl.gov/ smg/MOM.

Phillips, N. (1957). A coordinate system having some special advantages for numerical forecasting. *J.Met.*, 14:184–185.

Rattray Jr., M. (1982). A simple exact treatment of the baroclinicity-bathymetry interaction in a frictional, iterative, diagnostic ocean model. *J. Phys. Oceanogr.*, 12:997–1003.

Sarkisyan, A. and Ivanov, V. (1979). Joint effect of baroclinicity and bottom relief as an important factor in the dynamics of sea currents. *Bull. Acad. Sci. USSR, Atmos. and Oceanic Phys.*, 7:439–462.

Simons, T. (1979). On the joint effect of baroclinicity and topography. *J. Phys. Oceanogr.*, 9:1283–1287.

Treguier, A., Dukowicz, J. K., and Bryan, K. (1996). Properties of nonuniform grids used in ocean general circulation models. *J. Geophys. Res.*, 101(C9):20877–20881.

Udall, I. (1996). The MOMA ocean general circulation model: an overview. Internal Report 42, UK Universities Global Atmospheric Modelling Programme.

Appendix

A.1 Necessary Definitions

We will now employ a spherical coordinate system (r, ϕ, λ) where r is the radial coordinate, ϕ is the meridional coordinate (latitude), and λ is the zonal coordinate (longitude). To derive the two desired vorticity equations we require the radial component of the curl of a vector in spherical coordinates. Suppose we have a vector, $\vec{F} = F^{(r)}\hat{e}_r + F^{(\phi)}\hat{e}_\phi + F^{(\lambda)}\hat{e}_\lambda$, the radial component of its curl operator would be expressed as

$$\begin{aligned}\left(\vec{\nabla} \times \vec{F}\right) \cdot \hat{r} &= \frac{1}{a^2 \cos\phi} \begin{vmatrix} \hat{e}_r & a\hat{e}_\phi & a\cos\phi\hat{e}_\lambda \\ \frac{\partial}{\partial r} & \frac{\partial}{\partial \phi} & \frac{\partial}{\partial \lambda} \\ F^{(r)} & aF^{(\phi)} & a\cos\phi F^{(\lambda)} \end{vmatrix} \cdot \hat{r} \\ &= \frac{1}{a\cos\phi}\left[-F^{(\lambda)}\sin\phi + \frac{\partial F^{(\phi)}}{\partial \phi}\cos\phi - \frac{\partial F^{(\phi)}}{\partial \lambda}\right]\end{aligned}$$

We have assumed that a thin-shell approximation(Haidvogel and Beckmann, 1999) where the radial coordinate is given a fixed value of a.

The gradient operator expressed in our spherical coordinate system takes on the form (given that F is a scalar quantity)

$$\vec{\nabla F} = \frac{\partial F}{\partial r}\vec{e}_r + \frac{1}{a}\frac{\partial F}{\partial \phi}\vec{e}_\phi + \frac{1}{a\cos\phi}\frac{\partial F}{\partial \lambda}\vec{e}_\lambda$$

We define the depth-averaged horizontal current velocities and the depth-averaged

pressure as

$$U = \frac{1}{H}\int_{-H}^{\eta} u\,dz$$

$$V = \frac{1}{H}\int_{-H}^{\eta} v\,dz$$

$$P = \frac{1}{H}\int_{-H}^{\eta} p\,dz$$

where H is the ocean bottom surface and η is the free surface. Because of their large difference in magnitude we assume that $\eta + H \approx H$ for all points and only divide by H during the depth-averaging process.

Leibnitz's rule for integration is utilized in the creation of both vorticity equations and we take the form given by Jeffrey(1995). An example would the depth-averaged zonal derivative of the meridional current velocity v.

$$\frac{\partial V}{\partial \lambda} - \frac{1}{H}\left(v_{free}\frac{\partial \eta}{\partial \lambda} - v_{bot}\frac{\partial H}{\partial \lambda}\right) = \frac{1}{\eta + H}\int_{H}^{\eta}\frac{\partial v}{\partial \lambda}\,dz$$

Successive applications of Leibnitz's rule can be applied to a quantity. For example, suppose one wanted to determine the depth-average of the second order derivative, $\frac{\partial^2 U}{\partial t \partial \phi}$.

$$\frac{\partial U}{\partial t} - \frac{1}{\eta + H}u_{free}\frac{\partial \eta}{\partial t} = \frac{1}{H}\int_{H}^{\eta}\frac{\partial u}{\partial t}\,dz$$

$$\frac{\partial^2 U}{\partial t \partial \phi} - \frac{1}{\eta + H}\left(u_{free}\frac{\partial^2 \eta}{\partial t \partial \phi} - \frac{\partial u_{free}}{\partial \phi}\frac{\partial \eta}{\partial t} - \frac{\partial u_{free}}{\partial t}\frac{\partial \eta}{\partial \phi} + \frac{\partial u_{bot}}{\partial t}\frac{\partial H}{\partial \phi}\right) = \frac{1}{H}\int_{H}^{\eta}\frac{\partial^2 u}{\partial t \partial \phi}\,dz$$

A.2 Vorticity of the depth-averaged flow

Starting with the Navier-Stokes equation similar to that utilized in MOMA(Udall, 1996)

$$\frac{\partial \vec{u}}{\partial t} + f\hat{e}_r \times \vec{u} = -\frac{\vec{\nabla} p}{\rho_o} + \vec{\tau} + \vec{l} \tag{A.1}$$

where

$$\vec{l} = \vec{u} \cdot \nabla \vec{u} - \kappa \nabla^4 \vec{u}$$

contains the nonlinear advection and diffusion terms of the vector equation. Just like during our numerical experiments, we will assume that $\vec{G}$ is known and the depth-averaging and curl operations are performed directly on the field itself not its individual components. We also assume that the nonlinear field is continuous so that the curl and depth-averaging operations can be interchanged without consequence. Therefore the resulting vorticity term arising from the nonlinear fields will be the same in both vorticity equations derived.

Depth-averaging Equation A.1 yields

$$\frac{\partial U}{\partial t} - \frac{1}{H}\left(u_{free}\frac{\partial \eta}{\partial t}\right) + fV + \frac{\sec\phi}{a\rho_o}\left(\frac{\partial P}{\partial \lambda} - \frac{1}{H}\left(p_{free}\frac{\partial \eta}{\partial \lambda} - p_{bot}\frac{\partial H}{\partial \lambda}\right)\right) + \tau^{(\lambda)} = 0 \tag{A.2}$$

$$\frac{\partial V}{\partial t} - \frac{1}{H}\left(v_{free}\frac{\partial \eta}{\partial t}\right) - fU + \frac{1}{a\rho_o}\left(\frac{\partial P}{\partial \phi} + \frac{1}{H}\left(p_{free}\frac{\partial \eta}{\partial \phi} - p_{bot}\frac{\partial H}{\partial \phi}\right)\right) + \tau^{(\phi)} = 0 \tag{A.3}$$

The vorticity equation for the depth-averaged flow is the radial component of the vector curl of Equations A.2 and A.3. We will express the vorticity equation as the sum of four collections of terms as so

$$\text{Temporal} + \text{Coriolis} + \text{Pressure} + \text{Stress} + \text{Non Linear} = 0 \qquad \text{(A.4)}$$

The first four term collections are given the following definitions.

$$\begin{aligned}
\text{Temporal} \equiv \quad & -\frac{\partial U}{\partial t}\sin\phi + \frac{\partial^2 U}{\partial t \partial \phi}\cos\phi - \frac{\partial^2 V}{\partial t \partial \lambda} + \frac{\partial \eta}{\partial t}\frac{u(\eta)\sin\phi}{H} \\
& -\frac{\partial \eta}{\partial t}\left(\frac{\partial u(\eta)}{\partial \phi} - \frac{u(\eta)}{H}\frac{\partial H}{\partial \phi}\right)\frac{\cos\phi}{H} \\
& -\frac{1}{H}\frac{\partial \eta}{\partial t}\left(\frac{\partial v(\eta)}{\partial \lambda} - \frac{v(\eta)}{H}\frac{\partial H}{\partial \lambda}\right) \\
& -\frac{1}{H}\left(\frac{\partial^2 \eta}{\partial t \partial \phi}u(\eta)\cos\phi + \frac{\partial^2 \eta}{\partial t \partial \lambda}v(\eta)\right) \\
\text{Coriolis} \equiv \quad & -f\left[V\sin\phi - \frac{\partial V}{\partial \phi}\cos\phi - \frac{\partial U}{\partial \lambda}\right] + \Omega V\cos^2\phi \\
\text{Pressure} \equiv \quad & -\frac{1}{aH\rho_o}\left[J(\eta, p_{free}) - J(H, p_{bot})\right] \\
\text{Stress} \equiv \quad & -\tau^{(\lambda)}\sin\phi + \frac{\partial \tau^{(\lambda)}}{\partial \phi}\cos\phi - \frac{\partial \tau^{(\phi)}}{\partial \lambda}
\end{aligned}$$

The "Non Linear" collection is the numerical determination of the depth-averaged radial component of the curl of the nonlinear field.

We have expressed the coriolis parameter as $f \equiv 2\Omega\sin\phi$ where ϕ is latitude and Ω is the rate of rotation for the earth in radians per second. When one take the spatial derivative of f in the meridional direction we get

$$\frac{\partial f}{\partial \phi} = 2\Omega\cos\phi$$

which brings about the $2\Omega V \cos^2\phi$ term in the coriolis collection.

The stress field, $\vec{\tau}$, contains the influence from the internal and external stresses on the domain. However, when one depth-integrates the stress field from the free surface to the ocean-bottom, the sum of individual stress fluctuations can be expressed simply as the difference in stress applied to the upper and lower boundaries. I.e.

$$\int_{-H}^{\eta} \vec{\tau}\, dz \equiv \vec{\tau}_{FRICTION} - \vec{\tau}_{WIND}$$

where $\vec{\tau}_{WIND}$ is the wind stress applied to the sea surface and $\vec{\tau}_{FRICTION}$ is the stress occured along the ocean bottom due to friction. It is assumed that we have these two fields are at disposal and thus only the curl of the sum of these two fields is required to compute the required vorticity term.

A.3 Forming the barotropic vorticity equation

We start by forming a vorticity equation from the original Navier-Stokes equations. This is achieved by determining the radial component of vector curl of Equation A.1.

$$\begin{aligned} -\frac{\partial u}{\partial t}\sin\phi + \frac{\partial^2 u}{\partial t \partial \phi}\cos\phi - \frac{\partial^2 v}{\partial t \partial \lambda} - f\left[\frac{1}{a}\left(v\sin\phi - \frac{\partial v}{\partial \phi}\cos\phi\right) - \frac{\partial u}{\partial \lambda}\right] \\ + \frac{2\Omega}{a} v\cos^2\phi - \tau^{(\lambda)}\sin\phi + \frac{\partial \tau^{(\lambda)}}{\partial \phi}\cos\phi - \frac{\partial \tau^{(\phi)}}{\partial \lambda} = 0 \end{aligned} \tag{A.5}$$

Depth-averaging Equation A.5 gives us the desired barotropic vorticity equation. We again use our term grouping scheme in the final vorticity equation.

$$\text{Temporal} + \text{Coriolis} + \text{Stress} + \text{Non Linear} = 0 \tag{A.6}$$

There is no pressure group this time as $\vec{\nabla} \times \vec{\nabla} p = \vec{0}$. The "Temporal", "Stress" and "Non Linear" groups are the same as the those found in the vorticity equation for the depth-averaged flow derived in the last subsection (Equation A.4). The "Coriolis" group has the form

$$\begin{aligned}\text{Coriolis} \equiv -f & \left[\frac{1}{a}\left(V\sin\phi - \frac{\partial V}{\partial \phi}\cos\phi\right) - \frac{\partial U}{\partial \lambda}\right] + \frac{2\Omega}{a} V\cos^2\phi \\ & + \frac{f}{a}\left[\frac{\cos\phi}{a}\left(v(H)\frac{\partial H}{\partial \phi} - v(\eta)\frac{\partial \eta}{\partial \phi}\right) + \left(u(H)\frac{\partial H}{\partial \lambda} - u(\eta)\frac{\partial \eta}{\partial \lambda}\right)\right]\end{aligned}$$

A.4 Vorticity correction relation

To form a vorticity correction relation similiar to the one devised by Mertz and Wright(1992), we simply subtract Equation A.6 from Equation A.4.

$$\begin{aligned}\frac{1}{\rho_o}\left[J(\eta, p_{free}) - J(H, p_{bot})\right] & \\ = -\frac{f}{a}\left[\frac{\cos\phi}{a}\left(v(H)\frac{\partial H}{\partial \phi} - v(\eta)\frac{\partial \eta}{\partial \phi}\right) + \left(u(H)\frac{\partial H}{\partial \lambda} - u(\eta)\frac{\partial \eta}{\partial \lambda}\right)\right] & \quad \text{(A.7)}\end{aligned}$$